Applied Surface Science 690 (2025) 162623

Contents lists available at ScienceDirect

Applied Surface Science

journal homepage: www.elsevier.com/locate/apsusc

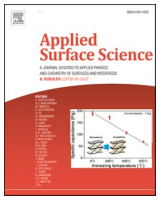

Full Length Article

Effect of Ag and Cu doping on the properties of ZnO magnetron sputtered thin films for biomedical applications

Ana-Marija Milisav [a], Maja Mičetić [a], Pavo Dubček [a], Lamborghini Sotelo [b,c], Cristina Cantallops-Vilà [d], Ina Erceg [a,e], Tommaso Fontanot [e], Krunoslav Bojanić [a], Željka Fiket [a], Maja Ivanić [a], George Sarau [e], Silke Christiansen [c,e], Edwige Meurice [d], Tihomir Car [a,*], Maja Dutour Sikirić [a,*]

[a] Ruđer Bošković Institute, Bijenička cesta 54, 10000 Zagreb, Croatia
[b] Friedrich-Alexander-Universität Erlangen-Nürnberg, Staudtstraße 7, 91058 Erlangen, Germany
[c] Innovations-Institut für Nanotechnologie und Korrelative Mikroskopie, Äußere Nürnberger Str. 62, 91301 Forchheim, Germany
[d] CERAMATHS, Université Polytechnique Hauts-de-France, 6 rue de Rambouillet, 59400 Cambrai, France
[e] Fraunhofer Institute for Ceramic Technologies and Systems IKTS, Äußere Nürnberger Str. 62, 91301 Forchheim, Germany

ARTICLE INFO

Keywords:
Magnetron sputtering
Calcium phosphate
Cytotoxicity
Biofilm
Antibacterial coating

ABSTRACT

Hospital-acquired infections are a major challenge for the healthcare system. The development of antibacterial surfaces for medical devices and non-critical surfaces in healthcare facilities is gaining attention as a promising strategy to prevent them. In this study, the properties of biodegradable magnetron-sputtered ZnO thin films doped with Ag and Cu were compared. In addition, biomimetic deposition of calcium phosphates (CaPs) on these surfaces was explored.

The investigated thin films doped were prepared by co-deposition in a multi-source magnetron sputtering system. X-ray diffraction of the prepared thin films revealed the formation of wurtzite in all cases. Grazing incidence small-angle X-ray scattering showed the formation of nanoparticles whose lateral-to-vertical diameter decreased with increasing Ag content and increased with increasing Cu content. The opposite influence of increasing Ag and Cu content in the thin films on grain size and water contact angle were also observed.

The biomimetic deposition of calcium phosphates (CaP) resulted in partial coverage of the surface of all thin films investigated with apatitic phase. CaP deposition resulted in a reduced WCA as well as a slightly reduced release of Cu and an increased release of Ag ions, while the release of Zn remained unaffected. Even though the tested surfaces exhibited cytotoxicity, CaP deposition enhanced MG-63 cell viability, especially for Ag-doped ZnO thin films, and improved the prevention of *S. aureus* and *P. aeruginosa* biofilm formation.

The results confirmed the potential of magnetron sputtering to coat materials for biomedical antibacterial applications and pointed to a viable strategy for preparing biocompatible surfaces.

1. Introduction

Despite advances in sterilization technologies and practices, hospital-acquired infections (HAIs) related to medical implants remain a serious healthcare problem, often leading to prolonged hospitalization, increased costs of treatment, and even patient death [1]. This issue is exacerbated by the increasing number of resistant bacterial strains [2]. Combating HAIs includes not only finding novel antimicrobial agents that are less likely to induce bacterial resistance but are also suitable for preventing bacterial adhesion and growth. A particular challenge in addressing this problem is the prevention of bacterial biofilm formation on the surfaces of medical devices and non-critical surfaces in medical facilities [3,4]. Biofilms, which consist of bacteria encapsulated in a self-secreted matrix, protect the bacteria and impair antibiotic efficacy, making infections difficult to treat [5].

To address this problem, different materials and strategies for

* Corresponding authors at: Laboratory for Thin Films, Division of Materials Physics, Ruđer Bošković Institute, Bijenička cesta 54, 10000 Zagreb, Croatia (T. Car); Laboratory for Biocolloids and Surface Chemistry, Division of Physical Chemistry, Ruđer Bošković Institute, Bijenička cesta 54, 10000 Zagreb, Croatia (M. Dutour Sikirić).

E-mail addresses: Tihomir.Car@irb.hr (T. Car), sikiric@irb.hr (M. Dutour Sikirić).

https://doi.org/10.1016/j.apsusc.2025.162623
Received 9 August 2024; Received in revised form 20 January 2025; Accepted 2 February 2025
Available online 3 February 2025

preparing antibacterial surfaces are being developed [6]. Among the different materials with antimicrobial activity for biomedical applications, metals and alloys are of special interest, as many biomedical devices (e.g., orthopedic implants and vascular stents) and non-critical surfaces in medical facilities are made of metals and alloys [7,8]. ZnO, Ag, and Cu are receiving special attention for the development of antimicrobial coatings due to their long-known antimicrobial activity [9,10] and low likelihood of inducing bacterial resistance, especially when used in nanostructured forms [11].

ZnO has several advantageous properties, including good chemical and mechanical stability, tunable band structures, high optical transparency, surface hydrophobicity, favorable biological properties, and low production costs [12]. Moreover, ZnO is a biodegradable metal, along with Mg and Fe [13]. It is used in a wide range of applications, such as rubber and textile production, agriculture, water purification, gas sensing, solar cells, LEDs, UV detectors, food packaging, photocatalysis, optoelectronic devices, biosensing, and bioimaging [14,15]. In, addition US Food and Drug Administration recognized ZnO as a safe material (21 CFR 182.8991) [16]. Despite its numerous biological functions, promising health implications, and pharmacological targets, research on ZnO for biomedical applications has been relatively limited [12,17]. Contrary, Ag and Cu have a long history of medical use [10,18]. Both materials have a broad spectrum of antimicrobial activity and are unlikely to cause bacterial resistance [10,19,20].

Magnetron sputtering is among the most frequently used techniques to grow thin films because a wide variety of thin films of high purity and low cost can be prepared. Another advantage of magnetron sputtering is co-deposition, which facilitates the mixing of thermodynamically immiscible materials, such as different binary metal combinations [21], enabling the preparation of a wide range of combinations of different materials. Also, materials obtained by magnetron sputtering often have different properties compared to the same materials obtained by other methods [22,23]. These advantages make the magnetron sputtering method of considerable interest for coating medical implant surfaces and non-critical surfaces in medical facilities.

The influence of experimental conditions on the properties of magnetron-sputtered ZnO thin films has been thoroughly studied [24,25]. Recently, doping ZnO thin films with Ag and Cu has attracted special attention as a possible way to improve their antibacterial properties. Although the preparation and properties of Ag- and Cu-doped ZnO thin films were previously reported [26–28], the potential for their application in biomedical purposes was not elaborated. In addition, despite the importance of the comparative studies of silver and copper containing surfaces prepared under the same experimental conditions, to the best of our knowledge, no comparison of the Ag and Cu doping on the properties of ZnO thin films has been made. Moreover, in general, comparisons of silver and copper containing surfaces are scarce [29].

To address these questions, the aim of this study was to determine and compare the influence of doping ZnO thin films with Ag and Cu on the physico-chemical properties of prepared films. In addition, the potential of prepared undoped and doped ZnO thin films for biomedical applications was tested by determining their cytotoxicity and ability to prevent biofilm formation. One major disadvantage of such thin films for biomedical applications is the lack of porosity, leading to poor osseointegration [30]. Therefore, the possibility of preparing biomimetic coatings with calcium phosphates (CaP) to enhance biocompatibility was also explored, as suggested for other materials [31–33]. The biomimetic method was chosen for its simplicity, cost-effectiveness, and ability to coat substrates of different shapes [34]. A two-step CaP deposition method was applied [31]. In the first step, the surface was activated by the adsorption of amorphous calcium phosphate (ACP). Subsequently, the samples were immersed in a metastable calcifying solution to promote the transformation from the amorphous to the crystalline phase.

2. Materials and methods

2.1. Materials

ZnO, Ag, and Cu targets, 99.99 % pure, were obtained from K. J. Lesker, USA. Argon, used as the discharge gas, was purchased from Messer, Croatia. The coatings were deposited on Si substrates obtained from University Wafer, USA.

The analytical grade calcium chloride ($CaCl_2$), sodium hydrogen phosphate (Na_2HPO_4), and hydrochloric acid (HCl) were obtained from Sigma Aldrich, Germany. HNO_3 (65 %, Suprapur®) was obtained from Merck, USA. The multielement reference standard and silver standard solution were obtained from Analytika, Czechia and Fluka, USA, respectively.

In biofilm assays, *Staphylococcus aureus* DSM 1104 and *Pseudomonas aeruginosa* DSM 22644 were used. Tryptic soy agar and tryptic soy broth were purchased from Biolife, D-(+)-glucose, phosphate buffer saline (PBS) and crystal violet 1 % solution from Sigma-Aldrich, Germany, API Suspension Medium® from BioMerieux, France and formaldehyde 35 % solution from Kemika, Croatia.

MG-63 cells (ECACC 86051601) purchased from Sigma-Aldrich, Germany, were used for cytotoxicity testing of prepared coatings. Minimum Essential Medium Alpha 1 (α-MEM) and dimethyl sulfoxide (DMSO) were purchased from Corning, USA, while Fetal Bovine Serum (FBS), amphotericin B, and gentamycin were purchased from PAN Biotech, Germany. For rinsing the cell culture wells Trypsin-EDTA, glutamine, and Dulbecco's Phosphate Buffered Saline (D-PBS) purchased from Dominique Dutscher, France were used. The MTT cell viability assay kit was purchased from Biotium, USA.

In all experiments, ultrapure water (UPW, conductivity 0.5 μS cm^{-1}, Hydrolab HLP 10 UV, Hydrolab, Poland) was used.

2.2. Preparation of magnetron-sputtered coatings

Thin Ag- and Cu-doped ZnO films were prepared by co-deposition in a multi-source magnetron sputtering system (CMS-18, K. J. Lesker, USA) at a working gas pressure $p(Ar) = 0.47$ Pa. Schematic representation of co-sputtering is shown in Fig. S1. Circular targets (Ø = 1 cm) were used, and samples were deposited at room temperature on Si substrates, with film thicknesses around 1 μm. ZnO thin films were either pure (ZnO) or doped with 3 at. %, 6 at. %, and 12 at. % of Ag (ZnOAg3, ZnOAg6, ZnOAg12, respectively) or Cu (ZnOCu3, ZnOCu6, ZnOCu12, respectively). For Ag-doped ZnO films, the magnetron power for the ZnO component was 150 W, with the magnetron power for the Ag cathode varying from 1 to 9 W, depending on the relative composition. For Cu-doped ZnO films, the magnetron power for the ZnO component was 140 W, with the power for the Cu cathode varying from 1 to 6 W, depending on the relative composition. Deposition times ranged from 90 to 120 min, depending on composition and magnetron power (Table S1).

Correspondingly, deposition rates of the composites varied from 0.14 nm/s to 0.17 nm/s ($ZnOCu_x$, $ZnOAg_x$). These rates were determined separately for each material by measuring the thickness of the deposited layer as a function of deposition time and source power. The cathode was positioned at an angle 14.5° relative to its plane. The distance of the substrate from the cathode plane was 0.17 m.

2.3. Biomimetic deposition of calcium phosphates

For biomimetic CaP deposition, stock solutions of $CaCl_2$ and Na_2HPO_4 (0.1mol dm^{-3}) were prepared by dissolving chemicals previously dried overnight in a desiccator over silica gel in UPW. The pH of the Na_2HPO_4 stock solution was adjusted to 7.4 with HCl.

Metastable calcifying solution (MCS) was prepared by rapidly mixing equal volumes of $5.6 \cdot 10^{-3}$ mol dm^{-3} $CaCl_2$ and $4.0 \cdot 10^{-3}$ mol dm^{-3} Na_2HPO_4 at pH = 7.4 solutions [31]. MCS was without detectable precipitate for at least 14 days when left undisturbed. A suspension of

amorphous calcium phosphate (ACP) was freshly prepared by rapidly mixing equal volumes of equimolar $CaCl_2$ and Na_2HPO_4 solutions with the initial reactant solutions $c(CaCl_2) = c(Na_2HPO_4) = 20{\cdot}10^{-3}$ mol dm^{-3}, pH = 7.4 [31].

For depositing CaPs a two-step procedure was applied [31]. To activate the magnetron-sputtered surfaces, samples were exposed to 3 mL of the freshly prepared ACP suspension for 7.5 min at room temperature, and the procedure was repeated three times. Subsequently, 3 mL of the MCS was poured over the samples to initiate the in-situ growth of nanocrystalline apatite. The samples were incubated for 48 h in a water bath at a temperature of 37 °C. In this way, CaP/ZnO, CaP/ZnOAg3, CaP/ZnOAg6, CaP/ZnOAg12, CaP/Cu3, CaP/Cu6 and CaP/Cu12 samples were prepared.

2.4. Characterization

2.4.1. X-ray diffraction (XRD)

X-ray diffraction patterns were recorded on PANalytical Aeris Research Edition (Malvern PANalytical, Malvern, Worcestershire, UK) in Bragg–Brentano geometry using CuKα radiation. Patterns were obtained in an angular scan range of 10° to 60° 2θ, with a scan rate of 1° min^{-1} and a step size of 0.02° 2θ. The sizes of crystallites were calculated using the Scherrer equation.

2.4.2. Grazing-incidence small-angle X-ray scattering (GISAXS)

GISAXS maps were measured at the SAXS beamline of the synchrotron Elettra Trieste, Italy, using a photon energy of 8 keV. The scattered radiation was collected by a two-dimensional Pilatus3 1 M detector. The grazing incidence angle was adjusted slightly above the critical angle of total reflection for the GISAXS measurements ensuring surface sensitivity of the measurement.

The lateral and vertical sizes of the nanoparticles were determined by numerical analysis of the GISAXS results, using procedure described in reference [35]. No correlation in the positions of the nanoparticles was assumed, i.e. only the nanoparticle shape was considered.

2.4.3. Atomic force microscopy (AFM)

The surface was probed by NT-MDT N'Tegra Prima AFM, which was operated in contact mode. 2 μm by 2 μm images of surface topography have been analyzed using Gwyddion 2.61 software.

2.4.4. Scanning electron microscopy (SEM) and energy dispersive spectroscopy (EDS)

The surface morphologies and microstructures of the magnetron-sputtered films, with and without CaP, were examined using a Zeiss Crossbeam 550 SEM (Germany) or a JEOL JSM-7000F FE-SEM (Tokyo, Japan). Imaging was performed at electron beam energies of 5 to 10 kV. EDS analysis was conducted using an Oxford Ultim Max 170 EDS detector (United Kingdom) integrated into the Zeiss Crossbeam 550 SEM at 20 kV to detect Zn, O, Ag, Cu, Ca, and P. For each sample, three regions of interest were analyzed. The grain sizes were determined from SEM micrographs using the open-source software ImageJ (http://imagej.nih.gov/ij/). The diameter of at least 50 particles was measured, and results are presented as mean with standard deviation.

Cross-sectional SEM micrographs were obtained using the Axia ChemiSEM (Thermo Fisher Scientific, USA) operated at a voltage of 10 kV and a 45° angle. Samples were sputter-coated with gold before analysis.

To prepare the samples after the biofilm formation assays for SEM visualization, samples were washed with PBS, fixed with 10 % formaldehyde, and dehydrated in ethanol series (70 % for 10 min, 80 % for 10 min, 90 % twice for 10 min, and 100 % overnight). Dried samples were sputter-coated with gold for SEM imaging [36].

2.4.5. Raman spectroscopy

Raman measurements were performed using Horiba LabRam Odyssey Nano (Horiba Scientific, Kyoto, Japan) Raman spectrometer with an optical microscope and a Nd-YAG laser operated with an excitation wavelength of 532 nm. Laser power varied depending on the samples type, and was 15.28 mW for CaP/ZnOCu3, 6.11 mW for the CaP/ZnO, CaP/ZnOAg3, CaP/ZnOAg6, ZnO, ZnOAg3, ZnOAg6, ZnOAg12, and ZnOCu3, and 3.06 mW for CaP/ZnOAg12. All the samples were imaged using 50 kX long working objective. The spectrometer was calibrated to a 520 cm^{-1}Si signal. The measurements were conducted with an accumulation time of 2 s and 200 accumulations.

2.4.6. Wettability

To evaluate the wettability of the coatings, static contact angle measurements were performed with the Krüss DSA25E goniometer (Germany). A 1 μL droplet of ultrapure water and 1 μL of diiodomethane were deposited on the surface of the magnetron-sputtered coatings, both with and without CaP, and then recorded with a camera. Measurements were taken for four droplets for each sample. The data obtained was then analyzed using Krüss Advance software.

Surface free energy (SFE) was calculated using the OWRK geometric mean theory [37]. The total surface free energy is a combination of dispersion forces (van der Waals forces) and polar forces (hydrogen bonding forces). Equations are as follows:

$$\gamma_L cos\theta = \gamma_S - \gamma_{SL} \quad (1)$$

$$\gamma_{SL} = \gamma_S + \gamma_L - 2\sqrt{\gamma_S^d \gamma_L^d} - 2\sqrt{\gamma_S^p \gamma_L^p} \quad (2)$$

$$\gamma_L(1 + cos\theta) = 2\sqrt{\gamma_S^d \gamma_L^d} + 2\sqrt{\gamma_S^p \gamma_L^p} \quad (3)$$

Eq. (1) represents Young's equation, which shows the relationship between interfacial tensions. Eq. (2) corresponds to the OWRK theory, while Eq. (3) combines both (1) and (2). In these equations, the variables γ_L, γ_S, and γ_{SL} represent the tensions at liquid/air, solid/air, and solid/liquid interfaces, respectively. γ^d and γ^p denote their dispersive and polar components. Mean contact angles of water and diiodomethane were used for the calculations.

2.4.7. Inductively coupled plasma mass spectrometry (ICP-MS)

To assess ion release from the samples, the substrates were immersed in 5 mL of PBS at 37 °C. Aliquots were collected for analysis at 1, 4, and 24 h. Each time an aliquot was removed, it was promptly replaced with fresh PBS. Prior to analysis, the collected solutions underwent a 100-fold dilution and were acidified with 2 % (v/v) HNO_3.

The total concentrations of Ag, Cu, and Zn were determined using the 8900 ICP-QQQ instrument from Agilent, USA. The concentrations of these elements were determined through external calibration using standard solutions. The standards were made by appropriately diluting a multi-element reference standard (100 ± 0.2 mg/dm^{-3}) containing Cu and Zn, and a single standard solution of Ag (1,000 ± 0.002 g/dm^{-3}).

The quality of the measurements was ensured by simultaneously analyzing blank samples and internal control samples. The samples were analyzed in triplicates, the results were normalized to the substrate surface and expressed as cumulative released mass per cm^2 of coating.

2.4.8. Bacterial adhesion and biofilm formation assay

Bacterial adhesion and biofilm formation on magnetron-sputtered thin films were investigated using *S. aureus* and *P. aeruginosa*. Before the testing in ambient conditions, the samples were sterilized under the UV lamp for 30 min. Three replicates per bacterial strain and two negative controls were prepared.

Bacterial inoculum was prepared from fresh overnight cultures on tryptic soy agar, adjusted to 0.5 MacFarland in 5 mL of 0.85 % API Suspension Medium®, and diluted to $5{\cdot}10^4$ CFU mL^{-1} in tryptic soy broth containing 1 % glucose. The samples were incubated with diluted inoculum in 24-well microplates overnight at 35 °C in an aerobic

atmosphere to promote bacterial growth and biofilm formation. After incubation, samples were washed three times with PBS, fixed with formaldehyde for 15 min, washed again, and stained with 0.1 % crystal violet for 15 min. Samples were then rinsed with PBS, dried at 60 C for 45 min, and immersed in 96 % ethanol for 30 min to resolubilize the bound crystal violet. A 100 µL aliquot of the obtained solution was transferred to a 96-well plate, and absorbance was measured at 590 nm (OD_{590}) using an Infinite 200 PRO microplate reader (TECAN, Grödig, Austria).

Mean absorbances and standard deviations were calculated. Biofilm formation (OD_{ratio}) was determined by dividing the mean absorbance of bacterial samples by the $OD_{cut\text{-}off}$ value (average blank values plus three times the standard deviations). For qualitative assessment, samples with $OD_{ratio} > 1$ are considered positive for biofilm formation and ≤ 1 as negative, i.e. no biofilm was formed. Quantification of biofilm formation was as follows: OD_{ratio} of 0–1 no biofilm, 1–2 weak biofilm, 2–4 moderate biofilm, and >4 strong biofilm formed [38,39].

2.4.9. Cytotoxicity assays

The human osteoblastic MG-63 cells were used to determine cytotoxicity of the thin films. Cells were cultured in 25 or 75 cm^2 flasks (Thermo Fisher Scientific, USA) in Minimum Essential Medium Alpha 1 supplemented with 10 % fetal bovine serum, 0.25 µg mL^{-1} amphotericin B, 2 mmol/L glutamine, and 50 µg mL^{-1} gentamicin. Cells were subcultured every 3–4 days when they reached 70 % confluence, using 0.05 % trypsin and diluting them in fresh media. Standard conditions, 37 °C, 5 % CO_2, in a humidified atmosphere, were utilized for cell incubation. Samples were sterilized by UV irradiation for 30 min.

Cytotoxicity was tested in two experimental setups: i) cells were seeded directly on untreated samples (unrinsed), and ii) cells were seeded on the samples that were exposed to cell culture media for 24 h (rinsed) [40]. In both setups, cells were seeded onto the sample surfaces at a density of $1{\cdot}10^5$ cells cm^{-2} in 24-well microplates (3524, Corning, USA) and cultured in media. Media with cells served as the positive control, while media without cells served as the negative control.

After 24 h of incubation, an MTT-containing medium was added, and cells were incubated for another three hours to allow the formation of formazan crystals. Crystals were dissolved with DMSO, and 100 µL aliquots of supernatant were transferred to a 96-well microplate (3596, Corning, USA). Absorbance was measured at 570 nm and 630 nm using the Infinite M200 PRO microplate reader (TECAN, Switzerland). Cell viability was calculated using Eq. (4):

$$\%viability = \frac{OD_{test} - OD_{blank}}{OD_{control} - OD_{blank}} \cdot 100 \quad (4)$$

where OD represents the optical density, i.e. (A_{570} – A_{630}) for each sample. OD_{blank} denotes the optical density of the negative control, while $OD_{control}$ refers to that of the positive control. Data were collected from six replicates for each sample. Statistical analysis was performed with Origin 9.0, utilizing non-parametric Kruskal-Wallis ANOVA followed by post-hoc Dunn's with a significance level of 0.05.

3. Results and discussion

3.1. Physico-chemical characterization of magnetron-sputtered coatings

The XRD diffraction patterns (Fig. 1) of all investigated thin films contained characteristic peaks of ZnO. In the diffraction pattern of undoped ZnO thin film, peaks at 2θ 31.8°, 34.2°, 36.0°, 47.5° and 56.6° were observed, corresponding to the (100), (002), (101), (102), and (110) reflections of hexagonal wurtzite (JCPDS Card No 89-1397). The sharp (002) reflection indicated the formation of a ZnO thin film with a *c*-axis orientation. The size of crystallites was 8.9 ± 1.5 nm. In addition, a peak characteristic of Si at 2θ 33.0° was observed in all samples.

No reflections characteristic of Ag and Cu were observed in the diffraction patterns of the doped thin films, indicating that either they were not deposited as separate phases or the amount of separate phases was not detectable by XRD. With the increase in Ag content, the relative intensity of the (002) reflection decreased compared to the (100) and (101) reflections, indicating a decrease in crystallinity, and a preferential orientation, as observed before [41,42]. In ZnOAg3 thin film, crystallites (23.8 ± 5.8 nm) larger than in ZnOAg6 and ZnOAg12 (12.6 ± 2.6 nm and 11.6 ± 2.1 nm, respectively) were formed. These results corroborate the previous study showing that the size of crystallites decreases with increasing silver content due to the degradation of the *c*-axis growth orientation [43].

In the diffraction patterns of the ZnOCu3 and ZnOCu6 samples, the (002) reflection was the only ZnO reflection detected. In contrast, sharp (100) and (110) reflections were observed in the pattern of the ZnOCu12 sample. The relative intensity of these reflections was higher than in the undoped ZnO thin film, indicating, as in the case of Ag doping, a decrease in film crystallinity and a preferential orientation. This is in accordance with previous findings, showing that doping ZnO thin films with Cu up to 5 % resulted in a decrease in crystallinity [44]. The crystallite size in (002) direction, although larger than in the pure ZnO thin film (11.4 ± 1.0 nm), decreased with increasing Cu content, being 40.3 ± 1.4 nm for ZnOCu3, 31.4 ± 2.7 nm for ZnOCu6, and 24.9 ± 2.1 nm for ZnOCu12.

GISAXS maps of Ag- and Cu-doped ZnO films are shown in Fig. 2. All measured maps showed signal originating from nanoparticles of

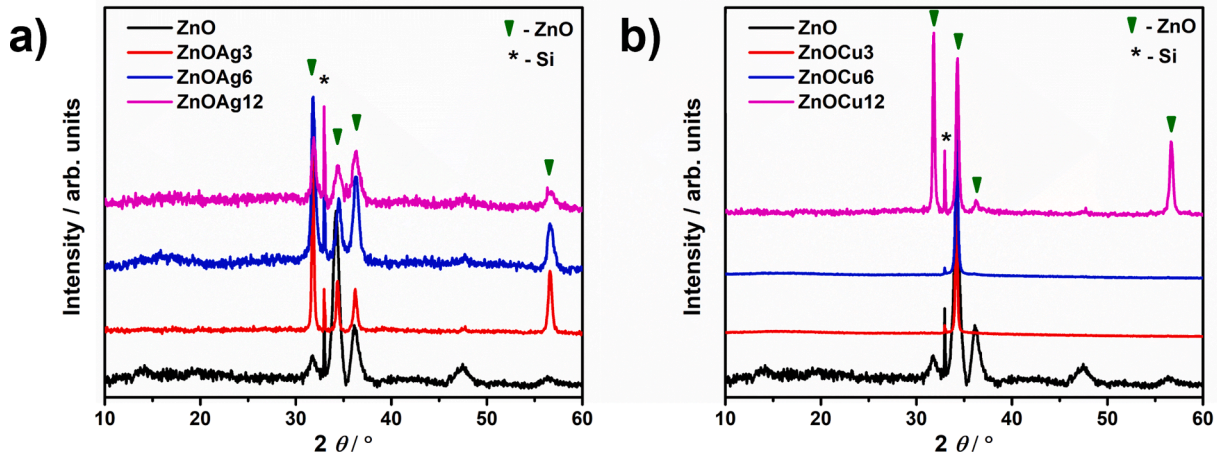

Fig. 1. X-ray diffraction patterns of ZnO thin films, undoped or doped with 3 at. %, 6 at. % and 12 at. % of a) Ag (ZnOAg3, ZnOAg6, ZnOAg12, respectively) and b) Cu (ZnOCu3, ZnOCu6, ZnOCu12, respectively).

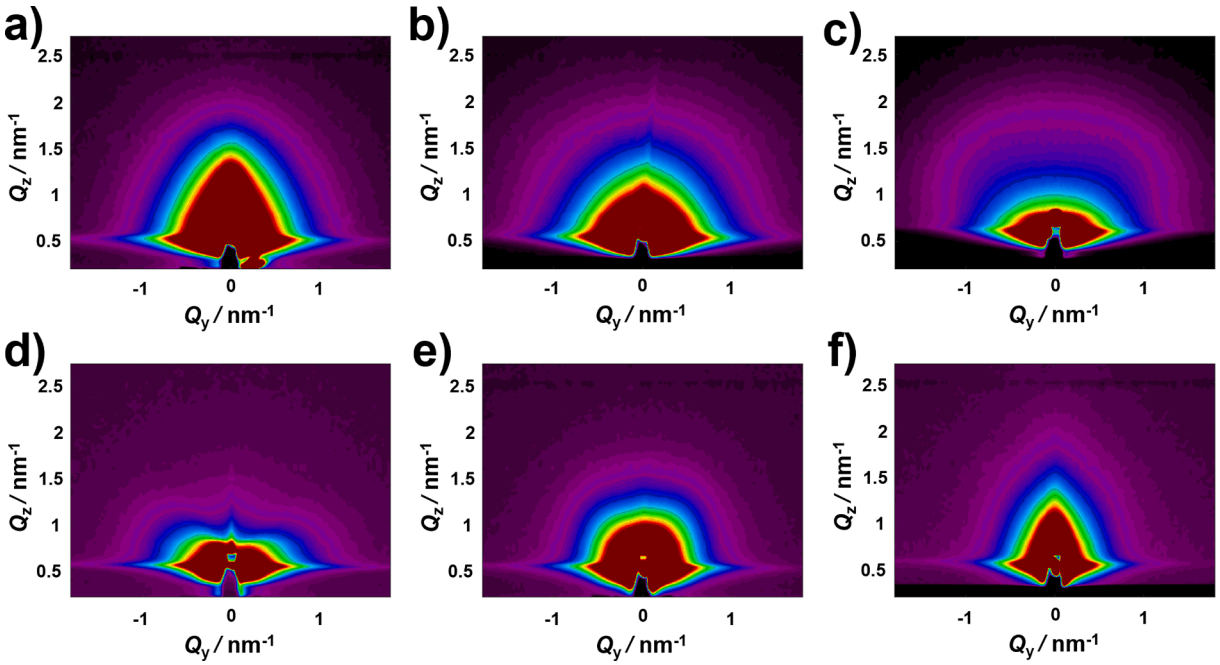

Fig. 2. GISAXS maps of ZnO thin films doped with 3 at. % (a, d), 6 at. % (b, e) or 12 at. % (c, f) of Ag (a-c) or Cu (d-f).

different shapes and sizes. The shape of the nanoparticle contributes to the GISAXS signal as its Fourier transform. Thus, the signal shape in the maps indicated the average shape of the nanoparticles in the reciprocal space. For the Ag-doped films (Fig. 2a–c) the ratio of lateral (parallel to the substrate) and vertical (perpendicular to the substrate) nanoparticle size is decreasing, while the opposite trend is observed for the Cu-doped films (Fig. 2d–f).

It was not possible to accurately determine the size distributions using only the GISAXS measurements because the beamstop obscured the central part of the maps (small Q_y and Q_z values). Additionally, the maps contained signals originating from the surface roughness at low Q values. This results in an excessive number of fitting parameters, making reliable quantitative analysis difficult. However, the lateral (parallel to the substrate) size of the formed nanoparticles was estimated from the SEM measurements, as shown in the next section (Table 2). These values were used as starting parameters for the fit of the GISAXS maps. D_L denotes the lateral size (parallel to the substrate), while D_V denotes the vertical size, the standard deviation of their distributions is denoted by σD (Table 1). Nearly spherical were formed at the highest applied concentration of silver, while in the case of copper they were formed at the lowest applied concentration. This indicated a different influence of Ag and Cu doping on the properties of investigated thin films.

The topography of the investigated thin films was visualized by AFM (Fig. 3). The ZnO thin films consisted of grains (Fig. 3a). Increasing the Ag content did not lead to significant changes in the topography or surface roughness (Fig. 3b–d, Table 2). On the contrary, an increase in grain size could be observed for Cu-doped ZnO thin films, resulting in substantially increased surface roughness of the ZnOCu6 and ZnOCu12 samples (Fig. 3e–g, Table 2).

The SEM micrographs of the magnetron-sputtered thin films are shown in Fig. 4. The undoped ZnO thin film exhibited characteristic irregular granular structures with an average diameter of 67.8 nm (Table 2), indicating the formation of columnar thin-film structures (Fig. 4) [16,24,45]. Cross-sectional SEM image revealed that a homogeneous and dense thin film was formed composed of columns with large diameters, similar to the ZnO thin films prepared by radio-frequency magnetron sputtering [3] was obtained. Shin et al. [24] have shown that the ZnO surface maintains a convex shape due to crystallite coalescence, where the diffusion rate of the atoms on the ZnO surface during columnar growth is lower than the deposition rate. The analysis of cross-section of ZnO thin films revealed that the structure of thin films is columnar [3,16,24]. The morphology depended on the deposition parameters, and columns extending from the bottom to the top of the layer have been observed [16,24], as well as a continuous structure [46].

Thin films doped with Ag showed a similar morphology to undoped ZnO thin films (Fig. 4). Contrary, previous findings suggested that in a reactive Ar-O_2 atmosphere, the shape of the columns changes from a circular columnar morphology to a triangular morphology at a very low Ag content. At the highest Ag content, gaps between the columns were observed [16], similar to our ZnOAg12 sample. Nevertheless, the grain diameter decreased with increasing Ag content (Table 2). Additionally, an increase in the number of small Ag particles between the grains was evident. These particles were likely not observed in the XRD patterns due to their small size and low surface concentration. Since Ag ions have a larger radius (0.122 nm) than Zn (0.074 nm), it is assumed that Ag^+ ions can substitute Zn^{2+} ions in the lattice, leading to either lattice distortion or segregation at the grain boundaries [47]. Segregation leading to the formation of nanoparticles, similar to that in this study, has been observed previously and explained by surpassing the solubility limit of Ag [45,48]. SEM cross-sectional images revealed that the columns extended from the substrate to the top of the layer and that their width increased at 12 % Ag. In addition, Ag nanoparticles could be observed sparsely at different depths. It was previously observed that the shape of the columns changes when Ag is added to thin ZnO films. Since

Table 1
Parameters of the GISAXS analysis of the nanoparticle sizes. Diameter in direction parallel to the substrate (D_L) and in the vertical direction (D_V), standard deviation of their distributions σ_D, and lateral-to-vertical ratio (D_L / D_V). All values are given in nm.

Sample	D_L / nm	D_V / nm	σD / nm	D_L / D_V
ZnOAg3	20	14	3	1.43
ZnOAg6	21	15	4	1.40
ZnOAg12	18	17	6	1.06
ZnOCu3	42	38	9	1.10
ZnOCu6	34	27	6	1.26
ZnOCu12	131	58	15	2.26

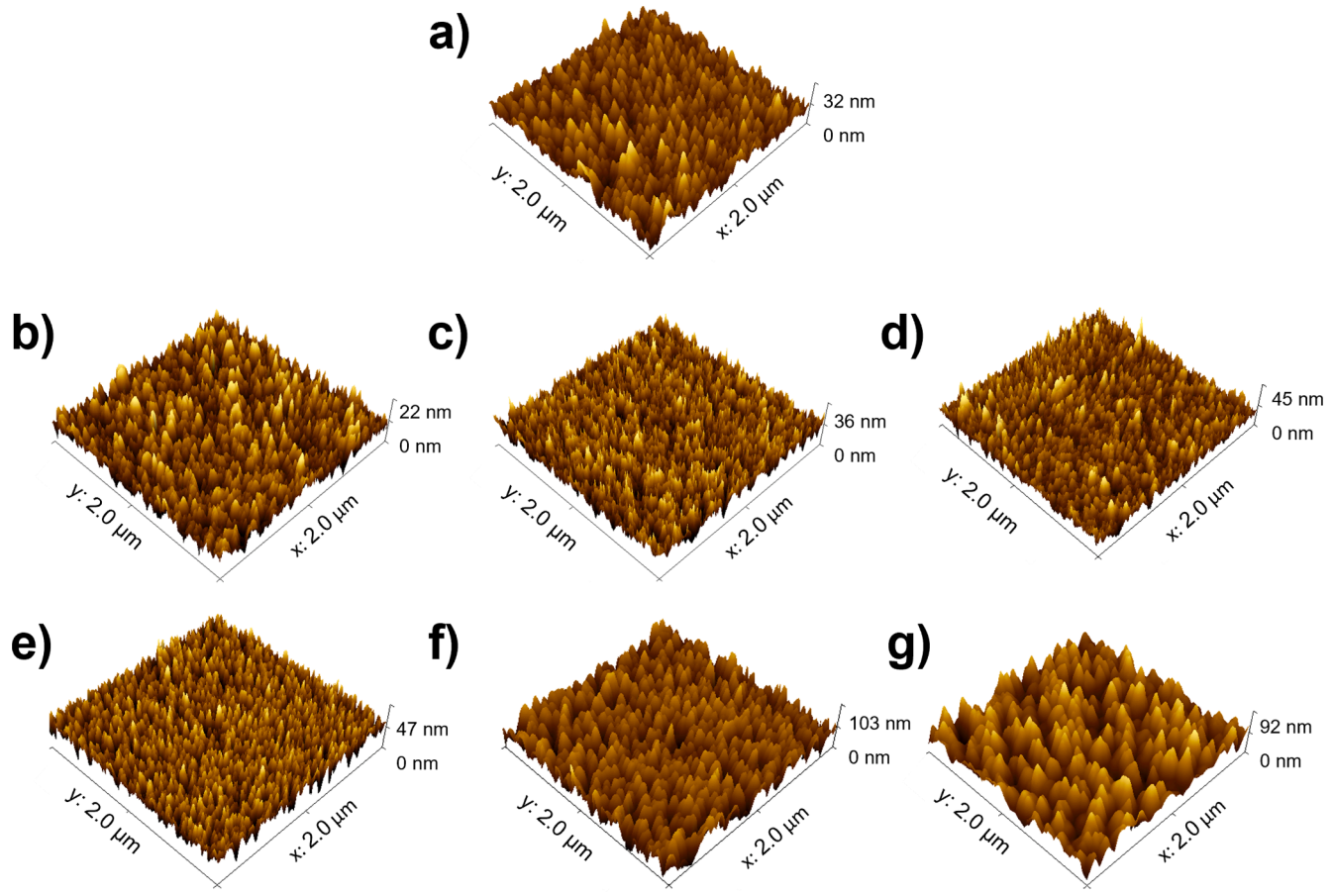

Fig. 3. AFM images of ZnO thin films, undoped (a) or doped with 3 at. % (b,e), 6 at. % (c,f) or 12 at. % (d-g) of Ag (b-d) or Cu (e-g).

Table 2
Surface roughness obtained from AFM images and grain size obtained from SEM images of ZnO thin films undoped or doped with 3 at. %, 6 at. % and 12 at. % of Ag (ZnOAg3, ZnOAg6, ZnOAg12, respectively) and Cu (ZnOCu3, ZnOCu6, ZnOCu12, respectively).

Sample	RMS (*Rq*) / nm	*Ra* / nm	d_{SEM} / nm
ZnO	4.2 ± 0.6	3.4 ± 0.5	67.8 ± 29.2
ZnOAg3	3.0 ± 0.1	2.4 ± 0.1	21.3 ± 6.5
ZnOAg6	4.0 ± 0.1	3.3 ± 0.3	20.1 ± 8.0
ZnOAg12	4.4 ± 0.1	3.5 ± 0.1	17.9 ± 5.9
ZnOCu3	5.8 ± 0.1	4.6 ± 0.1	46.4 ± 15.2
ZnOCu6	16.3 ± 0.9	13.2 ± 0.7	68.2 ± 23.0
ZnOCu12	14.4 ± 0.5	11.8 ± 0.4	132.9 ± 34.6

the columnar morphology is related to a preferential c-axis orientation, this could indicate that the presence of silver may cause a different crystalline growth, leading to a change in morphology [16].

In contrast, increasing Cu content resulted in a significant increase in grain diameter (Fig. 4, Table 2), in line with the obtained GISAXS results. SEM cross-sectional images (Fig. 4) revealed that irregular columns were formed, whose width increased with increasing Cu content. Khosravi et al. [46] observed that the structure changes from continuous to nanorod arrays for 3.4 % and 6.5 % Cu-doped ZnO thin films, while Piedade et al. [3] observed no effect of Cu doping. Cu is considered a favorable dopant because of its chemical and physical similarity to Zn, resulting in minimal lattice distortion [46]. The observed differences in physico-chemical properties between Ag and Cu-doped ZnO thin films point to a way of fine-tuning films properties for specific applications.

EDS maps provided further insights into the properties of the films (Fig. 4). The homogeneous distribution of Ag and Cu in all films indicated a successful incorporation of the dopants within ZnO thin films and a high degree of control in the thin film preparation process.

For orthopedic implants, the bioactivity of metal coatings is commonly enhanced by depositing a CaP layer [49]. A biomimetic deposition of CaP was performed to evaluate the biomedical applicability of the investigated magnetron-sputtered ZnO-based coatings.

SEM micrographs (Fig. 5) revealed that in all cases, CaP predominantly formed in the shape of aggregated spherical particles composed of thin leaf-like crystals, characteristic of the apatitic phase. These spherical particles only partially covered the film surface, suggesting that CaP formation resulted from the transformation of deposited ACP particles. The growth of CaP outside these areas, forming cloud-like patches, was rarely observed. Goel et al. [50] obtained similar results by depositing the apatite on co-sputtered Ti-ZnO nanocomposite thin films by immersing substrates in a Hanks Balanced Salt solution for two weeks at 37 °C. For CaP/ZnO and CaP/ZnOCu$_x$, some signs of magnetron-sputtered thin film disintegration were observed. In contrast, disintegration was less pronounced in the CaP/ZnOAg$_x$ films. However, round and rod-shaped nanoparticles containing Ag (Fig. S2, Supplementary Data) were detected on the surface between the CaPs, which became denser with increasing Ag content. At least some of these particles could be AgCl as its formation in the environment containing chloride ions is expected [51].

EDS analysis (Fig. S2, Supplementary Data) confirmed the presence of CaP, with the underlying magnetron-sputtered thin film remaining distinguishable between crystals.

To confirm the formation of CaPs, Raman spectroscopy was used (Fig. 6). As seen in the spectra of CaP/ZnO, CaP/ZnOAg$_x$, and CaP/ZnOCu$_x$ thin films, the bands corresponding to CaP were observed at around 430, 580, 962, and/or 1092 cm^{-1} [52,53]. For the CaP/ZnOCu$_x$

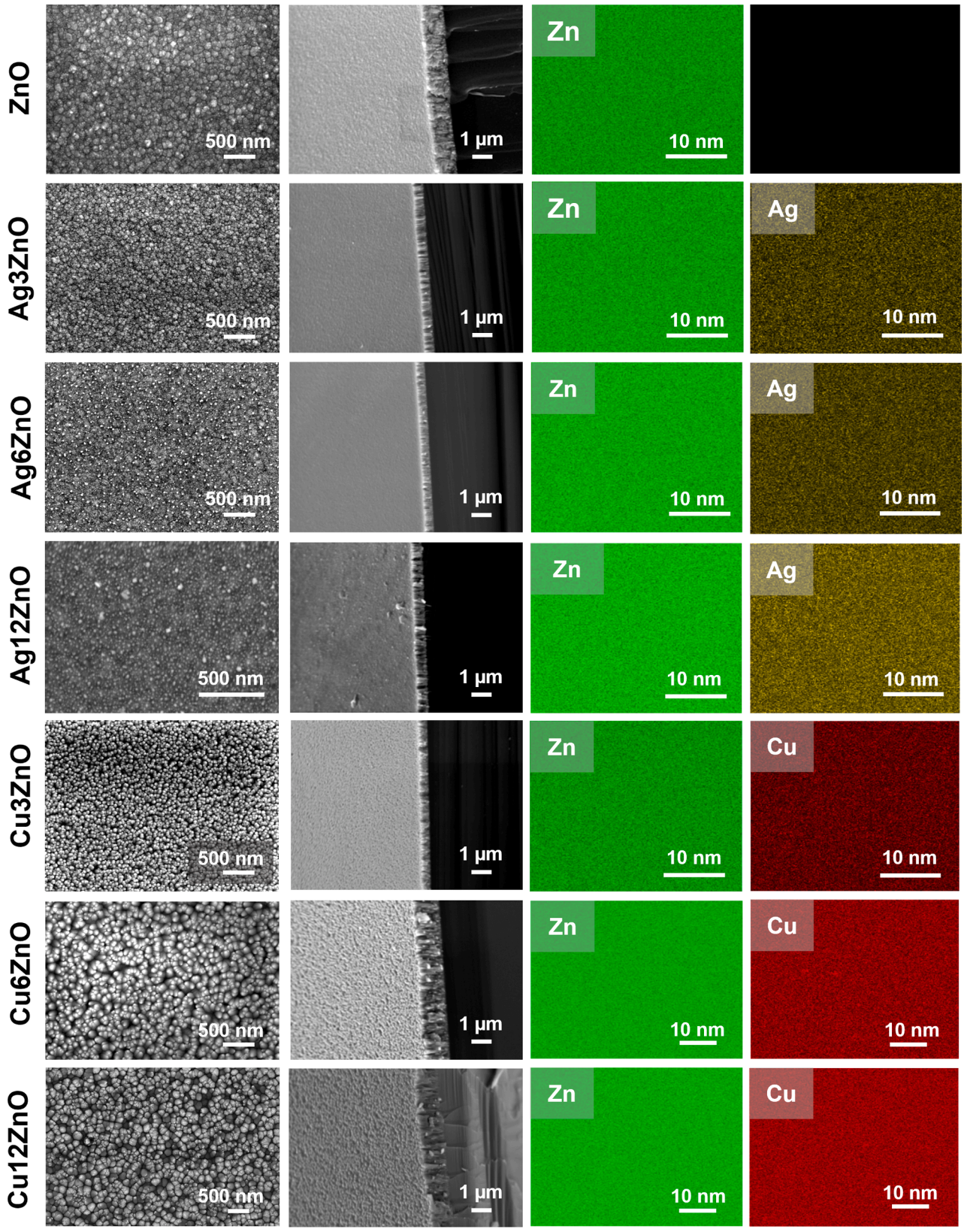

Fig. 4. SEM images (top view and cross-section) and EDS elemental distribution maps of ZnO thin films undoped or doped with 3 at. %, 6 at. % and 12 at. % of Ag (ZnOAg3, ZnOAg6, ZnOAg12, respectively) and Cu (ZnOCu3, ZnOCu6, ZnOCu12, respectively).

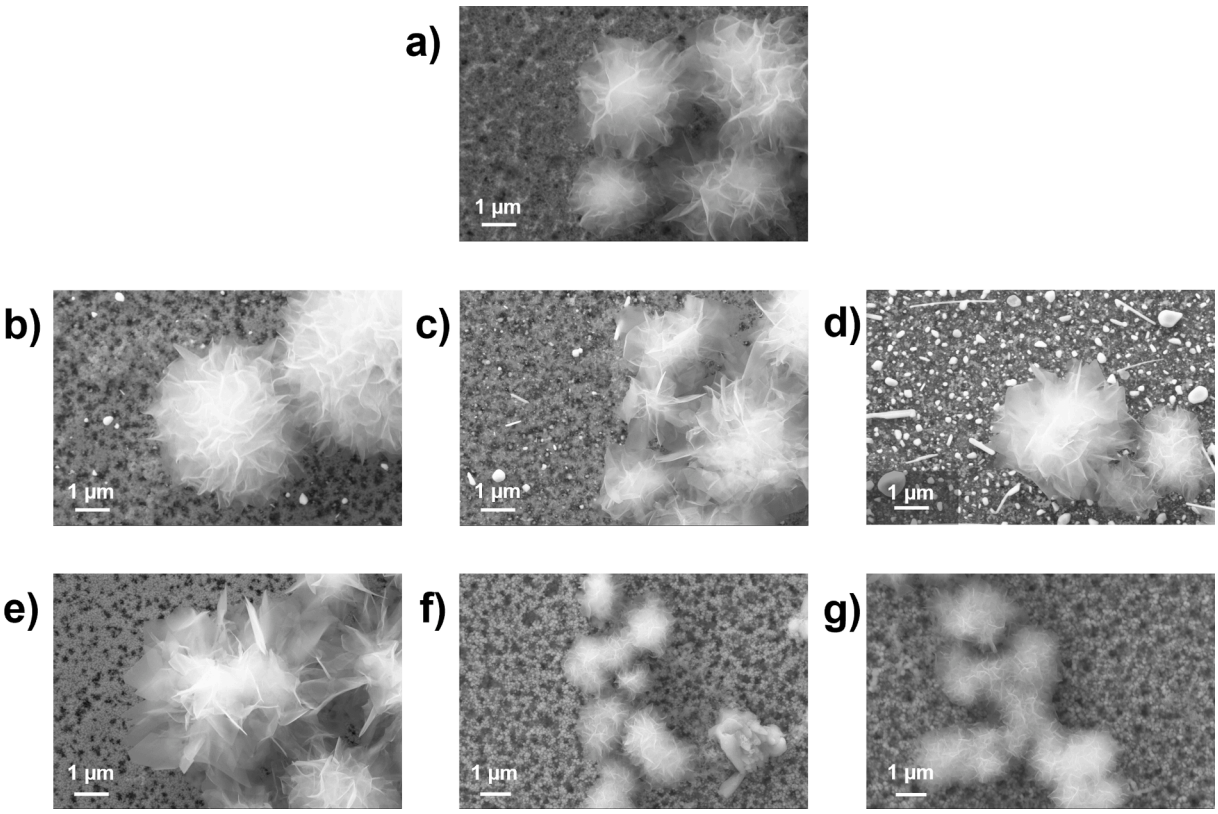

Fig. 5. SEM images of ZnO thin films, undoped (a) or doped with 3 at. % (b, e), 6 at. % (c, f) or 12 at. % (d-g) of Ag (b-d) or Cu (e-g) after biomimetic deposition of calcium phosphates.

thin films, only a low intensity peak was observed at around 1092 cm^{-1}, indicating that a small amount of CaP was formed. Given that CaPs were observed via optical imaging in the region where the Raman spectrum was recorded, it was possible that the CaP layer was too thin and thus only the Si substrate was measured. To explore this, a study of height profiles was performed (Fig. S3, Supplementary Data), which indicated that much thicker CaPs formed on Ag-doped films (average height 2.8 µm), compared to Cu-doped films (average height 0.5 µm).

In the Raman spectra of ZnO and Cu-doped ZnO thin films without CaPs, only bands characteristic of the Si substrate were detected (Fig. S4, Supplementary Data). It has already been reported that in the Raman spectrum of thin conductive oxide films like ZnO and CuO deposited on crystalline Si substrates, the dominant bands are from the 1st and 2nd order spectra of Si, as the Raman scattering cross-section of Si is much higher [54,55]. On the other hand, in the spectra of Ag-doped ZnO thin films, additional Raman bands were observed corresponding to the Ag-O and Ag-Ag vibrations of the Ag nanoparticles at around 234, 350 cm^{-1}, as well as a maximum shifting from 520 to 560 cm^{-1}, which may also correspond to the E_2 vibrational mode of ZnO [55–57]. Since SEM results indicated the formation of Ag nanoparticles, these bands can be attributed to Ag nanoparticles, as the shift of the maxima corresponds to the different sizes and morphologies of the nanoparticles.

The water contact angle (WCA) and surface free energy (SFE) are important physicochemical properties that offer insight into the wettability and adhesion of materials, which can influence their biological performance [58]. WCA measurements (Fig. 7a) indicated that all investigated thin films were hydrophobic, with only ZnOCu12 being slightly hydrophilic. Interestingly, the dopant content had opposite effects on the WCA for Ag and Cu. For Ag-doped ZnO films, wettability decreased with increasing Ag content, as evidenced by a WCA ranging from 102.8 ± 2.9° for ZnOAg3 to 117.5 ± 0.5° for ZnOAg12. Conversely, for Cu-doped ZnO surfaces, wettability improved with increasing Cu content, with the highest WCA of 119.9 ± 5.6° observed for ZnOCu3 and the lowest WCA of 85.7 ± 1.9° for ZnOCu12.

There is limited literature on the influence of Ag and Cu content on the wettability of ZnO thin films. Sapkal et al. [47] observed an increase in WCA with increasing Ag content up to 3 at. % in films prepared by spray pyrolysis, followed by a subsequent decrease in average grain size. Conversely, increasing the Ag content to 4 at. % led to an increase in grain size and a decrease in WCA. However, in this study, although grain size did not notably change with Ag-doping, the WCA consistently increased. Piedade et al. [3] showed a decrease in wettability upon Cu incorporation into ZnO thin films, attributing it to the formation of CuO on the film surface. In contrast, Chen et al. [59] observed that increasing the Cu content up to 6 at. % led to an increase in surface roughness, but a further increase to 10 at. % Cu resulted in decreased roughness. This trend was consistent with the changes observed in WCA, attributed to a higher volume of trapped air in the gaps on films with rougher surfaces, resulting in a larger air–water interface and, consequently, a higher WCA [60,61]. The results obtained in our study showed that the change of surface roughness with increasing Cu content from 6 at. % to 12 at. % was almost negligible, however, the WCA decreased.

The SFE of magnetron-sputtered films, calculated using the OWRK theory (Fig. 7b), ranged from 28.7 ± 4.2 mN m^{-1} (ZnOAg6) to 37.2 ± 0.4 mN m^{-1} (ZnOCu12), with slightly higher values observed for Cu-doped ZnO films. Increasing Ag content led to a decrease in SFE, while increasing Cu content resulted in a less pronounced increase in SFE. SFE values indicate solid–liquid interface interactions, providing insights into surface wettability – lower SFE is associated with weaker interactions with liquids, leading to higher contact angles and reduced wettability. This correlation is significant for predicting cell-surface interactions; surfaces with lower wettability tend to show less cell attachment and spreading [59,62]. In all cases, the dominant contribution to the total SFE was from the dispersive component.

The observed reduction in the WCA of magnetron-sputtered thin films with CaPs, compared to those without CaPs (Fig. 7a), suggests

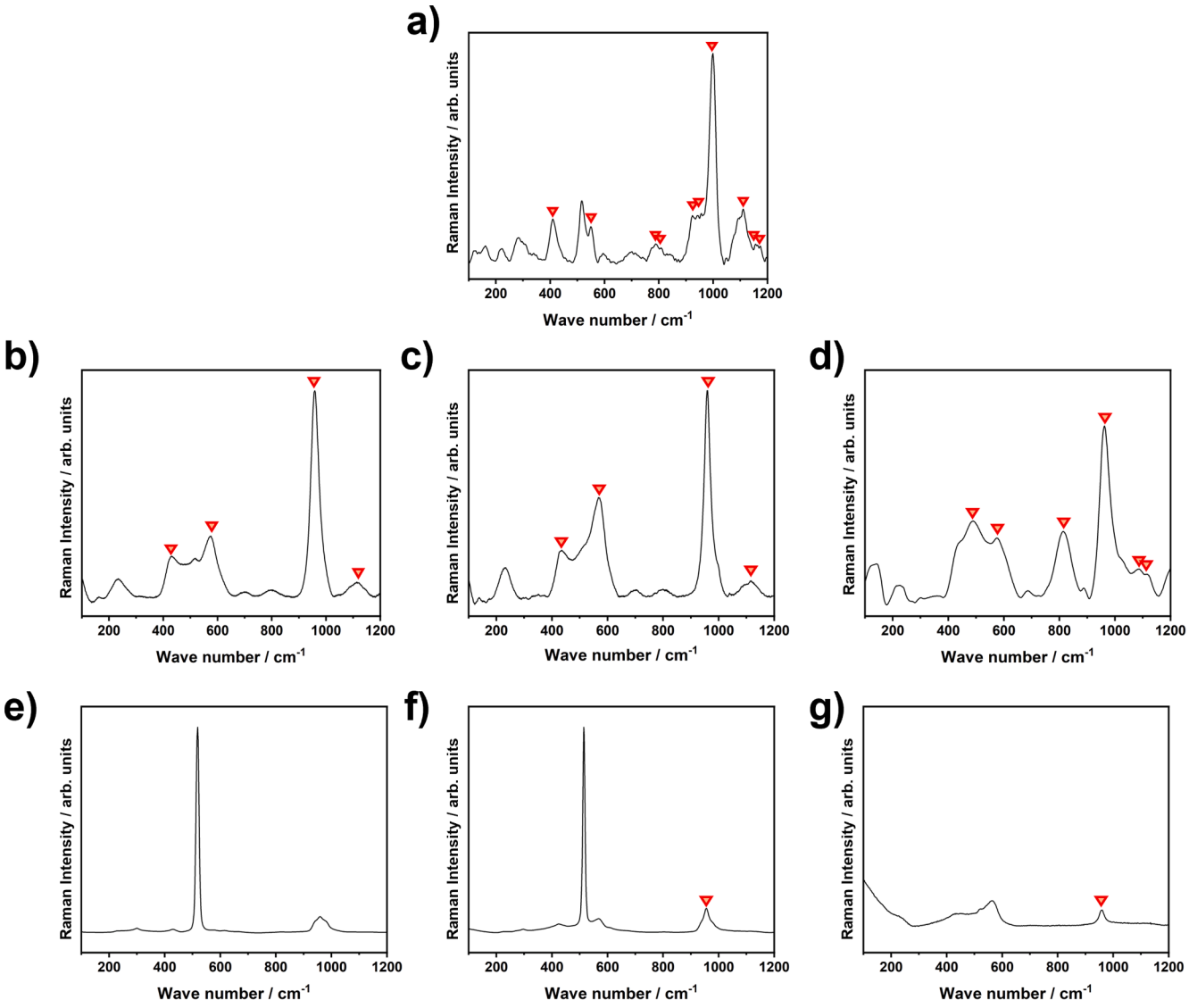

Fig. 6. Raman spectra of magnetron-sputtered thin films of ZnO thin films, undoped (a) or doped with 3 at. % (b,e), 6 at. % (c,f) or 12 at. % (d-g) of Ag (b-d) or Cu (e-g) after biomimetic deposition of calcium phosphates. CaP bands are denoted with triangles.

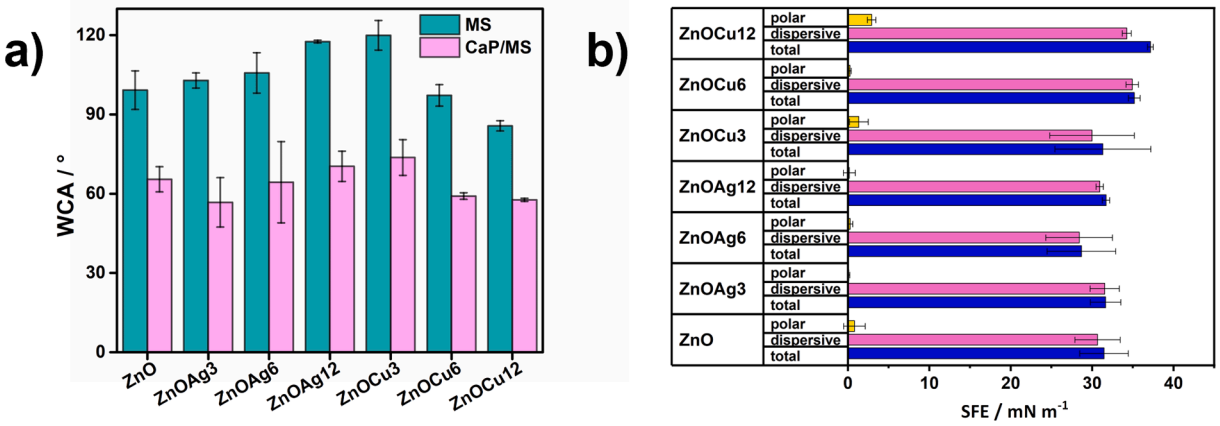

Fig. 7. a) Water contact angle (WCA) and b) surface free energy (total) and its dispersive (disperse) and polar (polar) component for magnetron-sputtered coatings undoped or doped with 3 at. %, 6 at. % and 12 at. % of Ag (ZnOAg3, ZnOAg6, ZnOAg12, respectively) and Cu (ZnOCu3, ZnOCu6, ZnOCu12, respectively), without (MS) and with deposited calcium phosphate (CaP/MS).

enhanced hydrophilicity, likely due to significant changes in surface topography. The high standard deviation of the measurements suggests notable variability, possibly as well reflecting observed heterogeneity of the surface. The SFE values for CaP-deposited samples are not shown due to high error, probably caused by the same reason.

One of the possible mechanisms of metal/metal oxides' antibacterial activity is ion release [63]. To the best of our knowledge, ion release studies from undoped and Ag- and Cu-doped ZnO thin films have not been performed so far. In this study, ion-release profiles in PBS were monitored at 37 °C for 24 h (Fig. 8), a duration aligned with biological characterization timelines. For all three ions (Ag^+, Cu^{2+}, and Zn^{2+}), an initial rapid release was observed within the first 4 h, followed by a gradual release up to 24 h. A similar behavior was previously reported for the release of Ag^+ ions from Ag-doped ZnO nanocomposites in powder form [64]. An exception was the ZnOAg12 film, where a decrease in Ag^+ ion concentration was observed. This phenomenon could be attributed to the precipitation of AgCl on the film surface in the presence of chloride-containing media [51]. This conclusion is also supported by the fact that despite the highest Ag content, the Ag^+ release from the ZnOAg12 film was the lowest (Fig. 8c). On the contrary, the release of Cu^{2+} ions increased with the increase of Cu content in the film (Fig. 8d).

After 24 h, the amount of Zn^{2+} ions released from the doped films was generally lower than that from the undoped film, except in the case of the ZnOCu6 film (Fig. 8a–b). No notable difference in Zn^{2+} release was observed between films with and without deposited CaP (Fig. 8a–b). However, the release of Ag^+ from Ag-doped ZnO samples with CaP was higher than from films without CaP (Fig. 8c). A reduction in the release of Ag^+ after 24 h was observed for all samples with CaP, probably due to the precipitation of AgCl. In contrast, the release of Cu^{2+} was somewhat higher for films without CaPs compared to their CaP-deposited counterparts (Fig. 8d).

3.2. Biofilm formation studies

Since the formation of biofilms can lead to detrimental health effects and prolong or restrict the treatment of infections [65], the formation of biofilms of Gram-negative *P. aeruginosa* and Gram-positive *S. aureus* was tested. These two bacterial strains are frequently associated with nosocomial infections, particularly with orthopedic implants [66,67].

The formation of *P. aeruginosa* biofilm on the pure ZnO thin film was almost completely inhibited, as evidenced by low $OD_{ratio,}$ whereas no inhibitory effect was observed for *S. aureus* (Fig. 9a). Interestingly, the addition of Ag at two lower contents considerably inhibited *S. aureus* biofilm formation, resulting in no or only weak biofilm formation (Fig. 9a). However, the inhibition of biofilm formation of *P. aeruginosa* was less efficient. At the highest Ag content, moderate *S. aureus* and strong *P. aeruginosa* biofilm were formed. Increasing Cu content resulted in an increased inhibition of *S. aureus* biofilm formation, while *P. aeruginosa* biofilm formation was almost completely inhibited, except for the ZnOCu6 thin film. The obtained results are in line with previous studies showing that copper and silver thin films exhibit differences in antiviral and antibacterial properties [29]. Interestingly, although ionic Ag is more efficient than ionic Cu, while Cu is more efficient than Ag when present in solid thin films. This was ascribed to a lower susceptibility of Ag to surface oxidation [29,68] compared to Cu, which retains its activity even after oxidation [68].

The results shown in Fig. 9b reveal that the deposition of CaP led to lower OD_{ratio} values, indicating better inhibition of biofilm formation of one or both bacterial strains on all samples (with the exception of ZnOAg12 and ZnOCu12 for *S. aureus,* Fig. 9b) compared to the samples without CaP. The Ag release was improved for the thin films with CaP (Fig. 8c), which could account for their better antibacterial activity. However, this was not the case for $ZnOCu_x$ thin films, indicating possible different mechanisms of action.

SEM micrographs (Figs. 10 and 11) provided detailed visualizations of the biofilm formation of *S. aureus* and *P. aeruginosa*. Both individual cells and clusters of *S. aureus* cells were observed, with clustering being more pronounced on ZnOCu6 and CaP/ZnOAg6 (Fig. 10). These results suggest that the addition of CaP may reduce the effectiveness of the inhibitory effect of silver and promote biofilm formation, which is not the case with copper. *P. aeruginosa* cells were observed as individual or

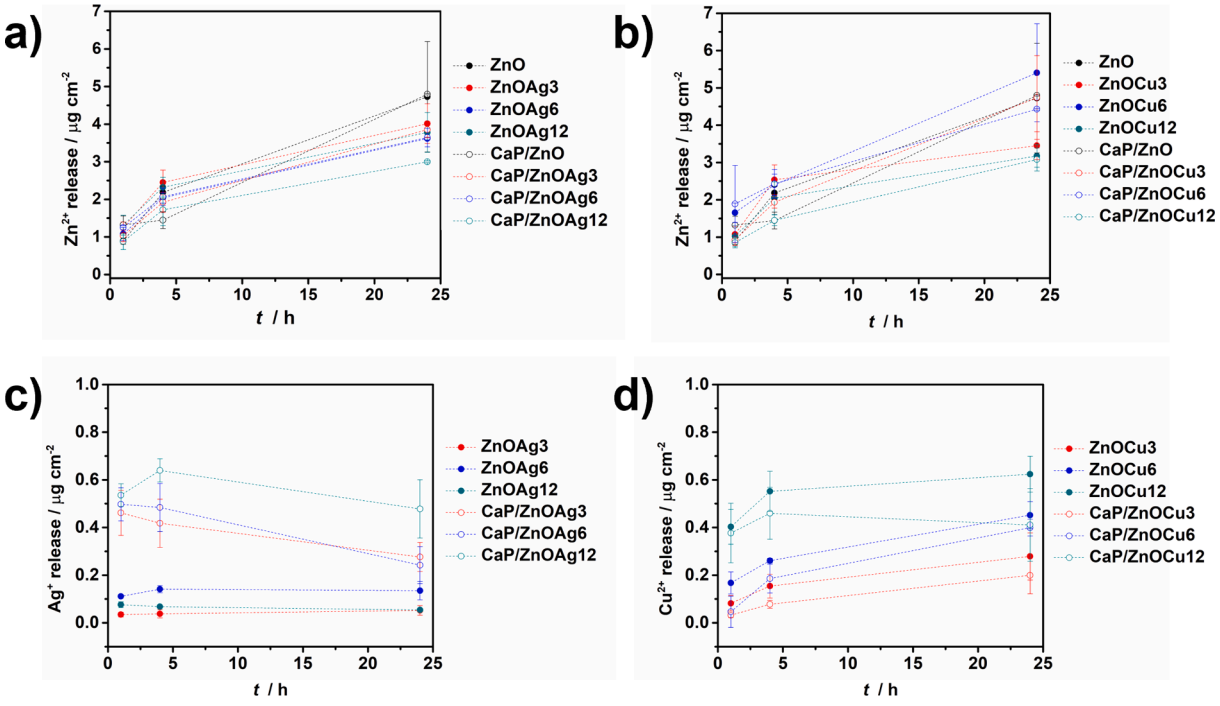

Fig. 8. Release of a-b) Zn^{2+}, c) Ag^+, d) Cu^{2+} during 1, 4, and 24 h from magnetron-sputtered thin films and magnetron-sputtered thin films undoped or doped with 3 at. %, 6 at. % and 12 at. % of Ag (ZnOAg3, ZnOAg6, ZnOAg12, respectively) and Cu (ZnOCu3, ZnOCu6, ZnOCu12, respectively) without or with calcium phosphates (CaP). The lines are only guidelines for the eye.

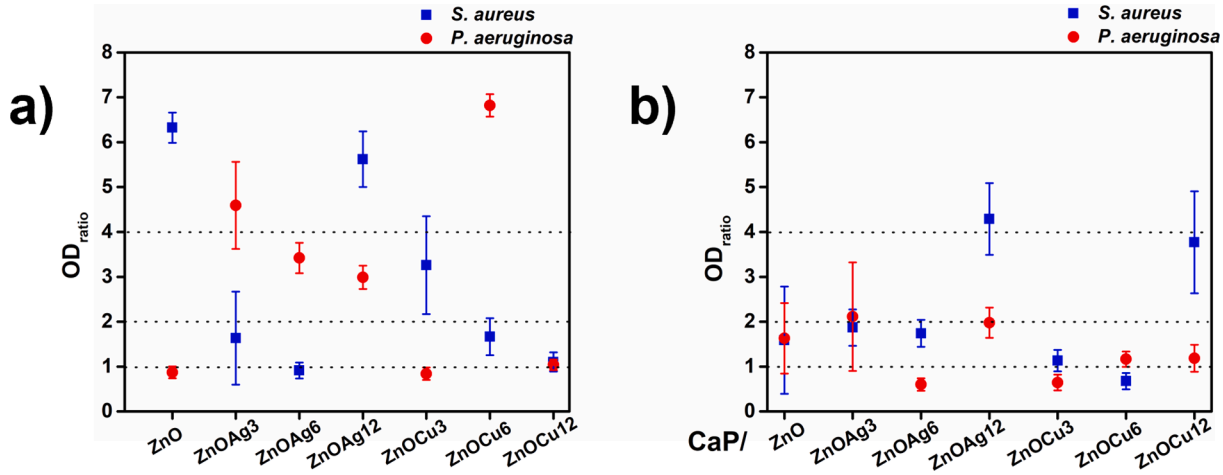

Fig. 9. Biofilm formation assay of *Staphylococcus aureus* and *Pseudomonas aeruginosa* on magnetron-sputtered thin films undoped or doped with 3 at. %, 6 at. % and 12 at. % of Ag (ZnOAg3, ZnOAg6, ZnOAg12, respectively) and Cu (ZnOCu3, ZnOCu6, ZnOCu12, respectively) a) without and b) with calcium phosphates (CaP). $OD_{ratio} \leq 1$ – no biofilm formed; $1 < OD_{ratio} \leq 2$ – weak biofilm formed; $2 < OD_{ratio} \leq 4$ – moderate biofilm formed; $4 < OD_{ratio}$ – strong biofilm formed. Dots represent the average values, and lines show the standard deviation.

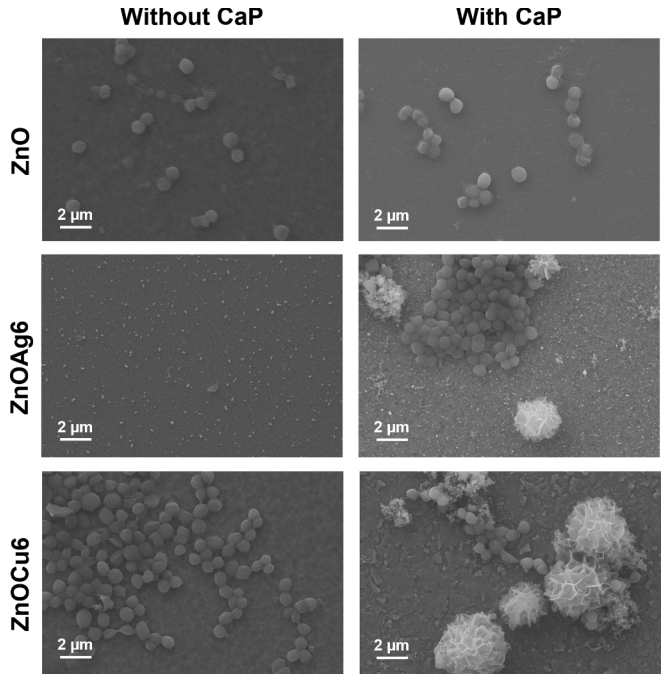

Fig. 10. Representative SEM images of *Staphylococcus aureus* biofilm formed on magnetron-sputtered ZnO thin films undoped or doped with 6 at. % of Ag (ZnOAg6) and Cu (ZnOCu6) without or with deposited calcium phosphates (CaP).

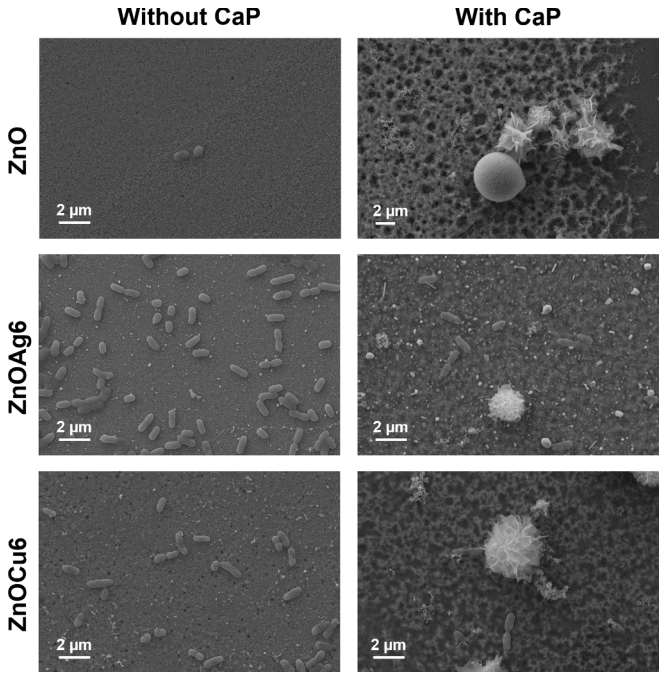

Fig. 11. Representative SEM images of *Pseudomonas aeruginosa* biofilm formed on magnetron-sputtered ZnO thin films undoped or doped with 6 at. % of Ag (ZnOAg6) and Cu (ZnOCu6) without or with deposited calcium phosphates (CaP).

scattered cells with minimal clustering. In some instances, cells with a coccoid morphology can be observed, indicative of impaired growth (Fig. 11). Although the quantitative assay for CaP-deposited samples showed lower OD_{ratio} values indicative of less total biomass, SEM micrographs showed some cell clustering and biofilm formation, especially for Ag-doped ZnO films. Conversely, Cu-doped ZnO films maintained better overall inhibition of biofilm formation. Important to note is that the direct visualization of surface biofilms with SEM is the most sensitive method, thus, the presence of a single or a few scattered bacterial cells (observed with SEM) could be undetectable by crystal violet assay.

The antimicrobial effect of both undoped and doped magnetron-sputtered ZnO thin films has been investigated in a number of studies, determining the influence of thin film composition, its structure, and thickness on antibacterial activity. Carvalho et al. [16] demonstrated that the antibacterial activity of magnetron-sputtered ZnO thin films against *E. coli* depends on the film thickness, with films between 200 and 600 nm showing the best performance. In our study, thicker ZnO films of 1 μm were used, and an inhibitory effect was observed, indicating that film thicknesses above 600 nm may also be effective. They also found that antibacterial activity increases with higher Ag content, similar to our results for up to 6 at. % Ag. Chuang et al. [69] showed that ZnO thin films containing 45 wt% of Ag_2O have a bacterial effect similar to the pure Ag_2O, while Geetha et al. [70] showed better inhibition of *S. aureus* adhesion upon doping ZnO with 69–88 % of Ag. In both these studies, a much larger silver content, compared to our study, was needed for the antibacterial effect to be observed. Vibornijs et al. [71] reported that

ZnO and three-layered ZnO-Cu-ZnO coatings exhibited low activity against *E. coli* and *S. aureus,* unlike pure Cu thin film, which showed high inhibitory activity, demonstrating the potent properties of Cu that can be hindered in such layered coatings due to slow release of Zn ions. Conversely, Goel et al. [50] found that co-sputtered Ti-ZnO nanocomposite films inhibited the growth of both bacterial strains. Meister et al. [29] showed that sequentially or co-deposited Ag/Cu nano patches effectively prevent bacterial growth after 24 h. Pure Ag or Cu nano patches have not shown this effect, which was explained by insufficient ion release. The increased ion release of Ag/Cu nano patches was ascribed to electrochemically driven enhanced dissolution and the possible combined effect of two antimicrobial metals.

3.3. Cytotoxicity evaluation

To further evaluate the potential of thin films prepared by magnetron sputtering for biomedical applications, thin films doped with 6 at. % Ag or Cu, with or without deposited CaPs, were selected for cytotoxicity evaluation. These films showed the best inhibition of bacterial biofilm formation and contained similar amounts of dopants. The cytotoxicity of MG–63 cells was determined in two experimental setups. In the first setup, the cells were seeded directly onto the samples (unrinsed). In the second setup, the samples were first exposed to cell culture media for 24 h, and subsequently, the cells were seeded on such rinsed samples.

The results of the MTT assays are shown in Fig. 12, indicating that there was no statistically significant difference in the viability of MG-63 cells between the two experimental setups. However, the viability was below 70 %, the threshold for non-cytotoxic materials according to the criteria of the ISO 10993–5. Despite this, the results revealed interesting behavior. The Ag-doped thin films had lower cytotoxicity than the pure ZnO and Cu-doped ZnO films. The addition of CaP improved the cell viability, although not statistically significant. The viability of the CaP-deposited ZnOAg6 thin film was 64.5 % for rinsed and 55.3 % for unrinsed, which was not statistically significantly different from the viability of the control cells according to the non-parametric Dunn's test.

For nanoparticles, the toxicity of the material usually correlates with ion release. It has already been shown that Zn^{2+} ions are toxic to rodent 3 T3 fibroblasts and the mesothelioma MSTO-211 cell lines at a concentration of 10 ppm [72], which is higher than the amount of Zn^{2+} ions released in our study (mostly below 1 ppm). On the other hand, silver nanoparticles above 50 μg mL^{-1} has been shown to be cytotoxic to MG-63 cells [73]. Hallab et al. [74] have shown that Cu is among the most toxic metals to MG-63 cells, with an LC50 of about 0.05 to 0.3 mM. Although the results of nanoparticle cytotoxicity studies can give insight into the mechanism of action, they should be used with caution in the explanation of thin film behavior. Cytotoxicity depends on the properties of the material, the type of cells used for the assays, and the type of assay performed [13]. In addition, cellular uptake, electrostatic and steric interactions of nanoparticles should also be taken into account [29]. Making comparison even more difficult is the fact that the concentrations of metal ions released from the coatings, which is considered one of the main mechanisms of cytotoxicity, are expressed in different ways.

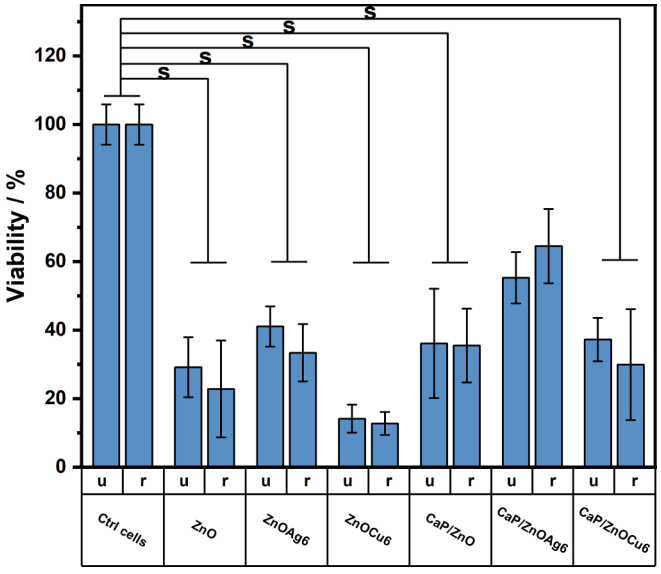

Fig. 12. Cell viability of MG-63 cells on magnetron-sputtered ZnO thin films undoped or doped with 6 at. % of Ag (ZnOAg6) and Cu (ZnOCu6) without or with deposited CaP (CaP/ZnO, CaP/ZnOAg6 and CaP/ZnOCu6, respectively). Error bars represent standard deviation. u – unrinsed and r – rinsed tested surfaces. Significant differences are denoted (s).

To the best of our knowledge, no cytotoxicity testing was performed for Ag and Cu doped ZnO thin films. Although numerous studies have investigated the antimicrobial activity of thin films containing ZnO, Ag, and/or Cu, few studies have examined their cytotoxicity. Goel et al. [50] studied magnetron-sputtered Ti-ZnO thin films containing 38.1–57.1 wt % Zn on Si (1001) substrates and observed superior adhesion and proliferation of MG-63 and L929 fibroblasts on coated substrates compared to uncoated control substrates. No significant difference was observed in the viability of osteoblasts on nano-Ti and nano-Ti/Ag coatings [75]. Contrary, Ta(Zn)O films showed higher cytotoxicity towards MG-63 cells than Ta_2O_5 films [76]. Magnetron-sputtered Cu thin films were cytotoxic to L929 cells, but the addition of Ti reduced cytotoxicity, and thin films with less than 53 % Cu were not cytotoxic [77].

4. Conclusion

HAIs remain a major challenge in healthcare. Among various strategies to address this issue, the development of advanced antimicrobial surfaces for medical devices and non-critical surfaces in healthcare facilities is considered to be an effective solution. Due to the low cost, high quality of thin films, and the potential for industrial-scale deposition, magnetron sputtering attracts considerable attention for preparing antimicrobial thin films.

In this study, we investigated the differences in the physicochemical and biological properties of Ag- and Cu-doped ZnO thin films prepared by magnetron sputtering. To enhance their bioactivity, CaPs were biomimetically deposited. The results showed opposite trends in physicochemical properties, including nanoparticle and grain size and film wettability, with increasing concentrations of Ag and Cu. This could be explained by the difference in the size of Ag and Cu cations and their influence on the structure of ZnO. Although the biomimetic deposition of CaP resulted in sparsely formed CaP crystals, the difference in properties was observed in the thin films without CaP. Samples containing CaP were more hydrophilic, better inhibitors of *Staphylococcus aureus* and *Pseudomonas aeruginosa* biofilm formation, and less cytotoxic to MG-63 cells compared to thin films with no CaP.

Overall, our results indicate that magnetron-sputtered ZnO thin films doped with Ag and Cu in combination with biomimetic CaP deposition represents a viable strategy for developing antimicrobial surfaces and point to a method of increasing their biocompatibility. Future studies should focus on long-term performance evaluations to further explore potential biomedical applications.

CRediT authorship contribution statement

Ana-Marija Milisav: Writing – original draft, Visualization, Validation, Investigation, Formal analysis. **Maja Mičetić:** Formal analysis, Investigation. **Pavo Dubček:** Investigation, Formal analysis. **Lamborghini Sotelo:** Investigation. **Cristina Cantallops-Vilà:** Investigation, Formal analysis. **Ina Erceg:** Investigation. **Tommaso Fontanot:** Investigation, Formal analysis. **Krunoslav Bojanić:** Methodology, Investigation, Formal analysis. **Željka Fiket:** Methodology, Formal analysis.

Maja Ivanić: Investigation. **George Sarau:** Investigation, Formal analysis. **Silke Christiansen:** Supervision, Methodology. **Edwige Meurice:** Investigation, Formal analysis. **Tihomir Car:** Writing – review & editing, Writing – original draft, Validation, Supervision, Methodology, Conceptualization. **Maja Dutour Sikirić:** Writing – review & editing, Writing – original draft, Validation, Supervision, Methodology, Funding acquisition, Conceptualization.

Declaration of competing interest

The authors declare that they have no known competing financial interests or personal relationships that could have appeared to influence the work reported in this paper.

Acknowledgments

This work has received funding from European Union's Horizon 2020 research and innovation programme under the Marie Sklodowska-Curie Actions (H2020-MSCA-ITN) as part of the project AIMed-Antimicrobial Integrated Methodologies for Orthopedic applications (grant agreement no. 861138). We are grateful to EONEX for technical assistance.

Appendix A. Supplementary material

Supplementary data to this article can be found online at https://doi.org/10.1016/j.apsusc.2025.162623.

Data availability

Data will be made available on request.

References

[1] A. Despotovic, B. Milosevic, I. Milosevic, N. Mitrovic, A. Cirkovic, S. Jovanovic, G. Stevanovic, Hospital-acquired infections in the adult intensive care unit—epidemiology, antimicrobial resistance patterns, and risk factors for acquisition and mortality, Am. J. Infect. Control 48 (2020) 1211–1215, https://doi.org/10.1016/j.ajic.2020.01.009.
[2] E. Avershina, V. Shapovalova, G. Shipulin, Fighting antibiotic resistance in hospital-acquired infections: current state and emerging technologies in disease prevention, diagnostics and therapy, Front. Microbiol. 12 (2021) 707330, https://doi.org/10.3389/fmicb.2021.707330.
[3] A.P. Piedade, A.C. Pinho, R. Branco, P.V. Morais, Evaluation of antimicrobial activity of ZnO based nanocomposites for the coating of non-critical equipment in medical-care facilities, Appl. Surf. Sci. 513 (2020) 145818, https://doi.org/10.1016/j.apsusc.2020.145818.
[4] A. Sultana, M. Zare, H. Luo, S. Ramakrishna, Surface engineering strategies to enhance the in situ performance of medical devices including atomic scale engineering, IJMS 22 (2021) 11788, https://doi.org/10.3390/ijms222111788.
[5] A. Zhao, J. Sun, Y. Liu, Understanding bacterial biofilms: from definition to treatment strategies, Front. Cell. Infect. Microbiol. 13 (2023) 1137947, https://doi.org/10.3389/fcimb.2023.1137947.
[6] J. Hasan, R.J. Crawford, E.P. Ivanova, Antibacterial surfaces: the quest for a new generation of biomaterials, Trends Biotechnol. 31 (2013) 295–304, https://doi.org/10.1016/j.tibtech.2013.01.017.
[7] N. Korei, A. Solouk, M. Haghbin Nazarpak, A. Nouri, A review on design characteristics and fabrication methods of metallic cardiovascular stents, Mater. Today Commun. 31 (2022) 103467, https://doi.org/10.1016/j.mtcomm.2022.103467.
[8] T. Kim, C.W. See, X. Li, D. Zhu, Orthopedic implants and devices for bone fractures and defects: past, present and perspective, Eng. Regen. 1 (2020) 6–18, https://doi.org/10.1016/j.engreg.2020.05.003.
[9] A. Hamad, K.S. Khashan, A. Hadi, Silver nanoparticles and silver ions as potential antibacterial agents, J. Inorg. Organomet. Polym. 30 (2020) 4811–4828, https://doi.org/10.1007/s10904-020-01744-x.
[10] N. Bharadishettar, U.K. Bhat, D. Bhat Panemangalore, Coating technologies for copper based antimicrobial active surfaces: a perspective review, Metals 11 (2021) 711, https://doi.org/10.3390/met11050711.
[11] L. Wang, C. Hu, L. Shao, The antimicrobial activity of nanoparticles: present situation and prospects for the future, IJN 12 (2017) 1227–1249, https://doi.org/10.2147/IJN.S121956.
[12] V. Puspasari, A. Ridhova, A. Hermawan, M.I. Amal, M.M. Khan, ZnO-based antimicrobial coatings for biomedical applications, Bioprocess Biosyst. Eng. 45 (2022) 1421–1445, https://doi.org/10.1007/s00449-022-02733-9.
[13] Q. Liu, A. Li, S. Liu, Q. Fu, Y. Xu, J. Dai, P. Li, S. Xu, Cytotoxicity of biodegradable zinc and its alloys: a systematic review, JFB 14 (2023) 206, https://doi.org/10.3390/jfb14040206.
[14] P. Sharma, M.R. Hasan, N.K. Mehto, A. Deepak, J.N. Bishoyi, 92 years of zinc oxide: has been studied by the scientific community since the 1930s- An overview, Sens. Int. 3 (2022) 100182, https://doi.org/10.1016/j.sintl.2022.100182.
[15] M. Gartner, H. Stroescu, D. Mitrea, M. Nicolescu, Various applications of ZnO thin films obtained by chemical routes in the last decade, Molecules 28 (2023) 4674, https://doi.org/10.3390/molecules28124674.
[16] P. Carvalho, P. Sampaio, S. Azevedo, C. Vaz, J.P. Espinós, V. Teixeira, J. O. Carneiro, Influence of thickness and coatings morphology in the antimicrobial performance of zinc oxide coatings, Appl. Surf. Sci. 307 (2014) 548–557, https://doi.org/10.1016/j.apsusc.2014.04.072.
[17] A. Moezzi, A.M. McDonagh, M.B. Cortie, Zinc oxide particles: Synthesis, properties and applications, Chem. Eng. J. 185–186 (2012) 1–22, https://doi.org/10.1016/j.cej.2012.01.076.
[18] J.L. Falconer, D.W. Grainger, 1.4 Silver Antimicrobial Biomaterials, in: Comprehensive Biomaterials II, Elsevier, 2017, pp. 79–91, https://doi.org/10.1016/B978-0-12-803581-8.09293-6.
[19] M. Ip, S.L. Lui, V.K.M. Poon, I. Lung, A. Burd, Antimicrobial activities of silver dressings: an in vitro comparison, J. Med. Microbiol. 55 (2006) 59–63, https://doi.org/10.1099/jmm.0.46124-0.
[20] M.K. Rai, S.D. Deshmukh, A.P. Ingle, A.K. Gade, Silver nanoparticles: the powerful nanoweapon against multidrug-resistant bacteria: activity of silver nanoparticles against MDR bacteria, J. Appl. Microbiol. 112 (2012) 841–852, https://doi.org/10.1111/j.1365-2672.2012.05253.x.
[21] T. Car, J. Ivkov, M. Jerčinović, N. Radić, The relaxation processes in the Al-(Nb, Mo, Ta, W) binary amorphous thin films, Vacuum 98 (2013) 75–80, https://doi.org/10.1016/j.vacuum.2012.09.008.
[22] M. Hezam, N. Tabet, A. Mekki, Synthesis and characterization of DC magnetron sputtered ZnO thin films under high working pressures, Thin Solid Films 518 (2010) e161–e164, https://doi.org/10.1016/j.tsf.2010.03.091.
[23] A. Kołodziejczak-Radzimska, T. Jesionowski, Zinc oxide—from synthesis to application: a review, Materials 7 (2014) 2833–2881, https://doi.org/10.3390/ma7042833.
[24] J.W. Shin, J.Y. Lee, T.W. Kim, Y.S. No, W.J. Cho, W.K. Choi, Growth mechanisms of thin-film columnar structures in zinc oxide on p-type silicon substrates, Appl. Phys. Lett. 88 (2006) 091911, https://doi.org/10.1063/1.2174829.
[25] W. Yang, J. Liu, Z. Guan, Z. Liu, B. Chen, L. Zhao, Y. Li, X. Cao, X. He, C. Zhang, Q. Zeng, Y. Fu, Morphology, electrical and optical properties of magnetron sputtered porous ZnO thin films on Si(100) and Si(111) substrates, Ceram. Int. 46 (2020) 6605–6611, https://doi.org/10.1016/j.ceramint.2019.11.147.
[26] A.C. Saritha, M.R. Shijeesh, L.S. Vikas, R.R. Prabhu, M.K. Jayaraj, Growth and characterization of p-ZnO:Cu thin film and its homojunction application, J. Phys. D: Appl. Phys. 49 (2016) 295105, https://doi.org/10.1088/0022-3727/49/29/295105.
[27] A.D. Saragih, H. Abdullah, D.-H. Kuo, Study on the doping effect of Cu-Doped ZnO thin films deposited by co-sputering technique, J. Phys.: Conf. Ser. 1230 (2019) 012031, https://doi.org/10.1088/1742-6596/1230/1/012031.
[28] R. Ramadan, S. Dadgostar, M. Manso –Silván, R. Pérez-Casero, M. Hernandez-Velez, J. Jimenez, O. Sanchez, Silver-enriched ZnO:Ag thin films deposited by magnetron co-sputtering: post annealing effects on structural and physical properties, Mater. Sci. Eng. B. 276 (2022) 115558, https://doi.org/10.1016/j.mseb.2021.115558.
[29] T.L. Meister, J. Fortmann, M. Breisch, C. Sengstock, E. Steinmann, M. Köller, S. Pfaender, A. Ludwig, Nanoscale copper and silver thin film systems display differences in antiviral and antibacterial properties, Sci. Rep. 12 (2022) 7193, https://doi.org/10.1038/s41598-022-11212-w.
[30] M. Akhtar, S.A. Uzair, M. Rizwan, M.A. Ur Rehman, The improvement in surface properties of metallic implant via magnetron sputtering: recent progress and remaining challenges, Front. Mater. 8 (2022) 747169, https://doi.org/10.3389/fmats.2021.747169.
[31] M.D. Sikirić, C. Gergely, R. Elkaim, E. Wachtel, F.J.G. Cuisinier, H. Füredi-Milhofer, Biomimetic organic-inorganic nanocomposite coatings for titanium implants, J. Biomed. Mater. Res. A 89A (2009) 759–771, https://doi.org/10.1002/jbm.a.32021.
[32] M. Dutour Sikirić, R. Elkaim, S. Lamolle, H.J. Ronold, S.P. Lyngstadass, H. Füredi-Milhofer, F. Cuisinier, Biomimetic organic-inorganic nanocomposite coatings for titanium implants. II. biological "In Vitro" and "In Vivo" characterization, Key Eng. Mater. 330–332 (2007) 401–404, https://doi.org/10.4028/www.scientific.net/KEM.330-332.401.
[33] M. Dutour Sikirić, C. Gergely, F. Cuisinier, H. Füredi-Milhofer, Biomimetic organic-inorganic nanocomposite coatings for titanium implants: i. preparation, physicochemical and mechanical characterization, Key Eng. Mater. 330–332 (2007) 389–392, https://doi.org/10.4028/www.scientific.net/KEM.330-332.389.
[34] G. Falini, S. Fermani, The strategic role of adsorption phenomena in biomineralization: biomineralization, Cryst. Res. Technol. 48 (2013) 864–876, https://doi.org/10.1002/crat.201200711.
[35] I. Mekterović, G. Svalina, S. Isaković, M. Mičetić, GisaxStudio—an open platform for analysis and simulation of GISAXS from 3D nanoparticle lattices, Appl. Sci. 12 (2022) 9773, https://doi.org/10.3390/app12199773.
[36] R. Ali, K. El-Boubbou, M. Boudjelal, An easy, fast and inexpensive method of preparing a biological specimen for scanning electron microscopy (SEM), MethodsX 8 (2021) 101521, https://doi.org/10.1016/j.mex.2021.101521.

[37] F. Awaja, M. Gilbert, G. Kelly, B. Fox, P.J. Pigram, Adhesion of polymers, Prog. Polym. Sci. 34 (2009) 948–968, https://doi.org/10.1016/j.progpolymsci.2009.04.007.

[38] S. Stepanović, D. Vuković, V. Hola, G.D. Bonaventura, S. Djukić, I. Ćirković, F. Ruzicka, Quantification of biofilm in microtiter plates: overview of testing conditions and practical recommendations for assessment of biofilm production by staphylococci, APMIS 115 (2007) 891–899, https://doi.org/10.1111/j.1600-0463.2007.apm_630.x.

[39] S. Barkarmo, D. Longhorn, K. Leer, C.B. Johansson, V. Stenport, S. Franco-Tabares, S.A. Kuehne, R. Sammons, Biofilm formation on polyetheretherketone and titanium surfaces, Clin. Exp. Dent. 5 (2019) 427–437, https://doi.org/10.1002/cre2.205.

[40] V. Stranak, H. Wulff, H. Rebl, C. Zietz, K. Arndt, R. Bogdanowicz, B. Nebe, R. Bader, A. Podbielski, Z. Hubicka, R. Hippler, Deposition of thin titanium–copper films with antimicrobial effect by advanced magnetron sputtering methods, Mater. Sci. Eng. C 31 (2011) 1512–1519, https://doi.org/10.1016/j.msec.2011.06.009.

[41] N.-E. Sung, S.-W. Kang, H.-J. Shin, H.-K. Lee, I.-J. Lee, Cu doping effects on the electronic and optical properties of Cu-doped ZnO thin films fabricated by radio frequency sputtering, Thin Solid Films 547 (2013) 285–288, https://doi.org/10.1016/j.tsf.2012.11.046.

[42] P. Khosravi, F. Karimzadeh, H.R. Salimijazi, Y. Abdi, Structural, optical and electrical properties of co-sputtered p-type ZnO:Cu thin-films, Ceram. Int. 45 (2019) 7472–7479, https://doi.org/10.1016/j.ceramint.2019.01.039.

[43] F.-C. Liu, J.-Y. Li, T.-H. Chen, C.-H. Chang, C.-T. Lee, W.-H. Hsiao, D.-S. Liu, Effect of silver dopants on the ZnO thin films prepared by a radio frequency magnetron co-sputtering system, Materials 10 (2017) 797, https://doi.org/10.3390/ma10070797.

[44] C. Cai, H. Zhang, J. Xie, L. Ma, The characterization of Cu-doped ZnO thin films prepared by using radio-frequency reactive magnetron sputtering, J. Korean Phys. Soc. 70 (2017) 856–860, https://doi.org/10.3938/jkps.70.856.

[45] R. Francq, R. Snyders, P.-A. Cormier, Structural and Morphological study of ZnO-Ag thin films synthesized by reactive magnetron co-sputtering, Vacuum 137 (2017) 1–7, https://doi.org/10.1016/j.vacuum.2016.10.024.

[46] P. Khosravi, F. Karimzadeh, H.R. Salimijazi, Investigation of structural and optical properties of ZnO:Cu co-sputtered thin films, Mater. Res. Express 6 (2019) 116420, https://doi.org/10.1088/2053-1591/ab4493.

[47] R.T. Sapkal, S.S. Shinde, A.R. Babar, A.V. Moholkar, K.Y. Rajpure, C.H. Bhosale, Structural, morphological, optical and photoluminescence properties of ag-doped zinc oxide thin films, Mat. Exp. 2 (2012) 64–70, https://doi.org/10.1166/mex.2012.1049.

[48] S.-T. Kuo, W.-H. Tuan, J. Shieh, S.-F. Wang, Effect of Ag on the microstructure and electrical properties of ZnO, J. Eur. Ceram. Soc. 27 (2007) 4521–4527, https://doi.org/10.1016/j.jeurceramsoc.2007.02.215.

[49] Y. Su, I. Cockerill, Y. Zheng, L. Tang, Y.-X. Qin, D. Zhu, Biofunctionalization of metallic implants by calcium phosphate coatings, Bioact. Mater. 4 (2019) 196–206, https://doi.org/10.1016/j.bioactmat.2019.05.001.

[50] S. Goel, P. Dubey, S. Ray, R. Jayaganthan, A.B. Pant, R. Chandra, Co-sputtered antibacterial and biocompatible nanocomposite titania-zinc oxide thin films on Si substrates for dental implant applications, Mater. Technol. 34 (2019) 32–42, https://doi.org/10.1080/10667857.2018.1488924.

[51] H. Wu, X. Xie, J. Wang, G. Ke, H. Huang, Y. Liao, Q. Kong, Biological properties of Zn–0.04Mg–2Ag: a new degradable zinc alloy scaffold for repairing large-scale bone defects, J. Mater. Res. Technol. 13 (2021) 1779–1789, https://doi.org/10.1016/j.jmrt.2021.05.096.

[52] I.A. Karampas, C.G. Kontoyannis, Characterization of calcium phosphates mixtures, Vib. Spectrosc 64 (2013) 126–133, https://doi.org/10.1016/j.vibspec.2012.11.003.

[53] M. Głąb, S. Kudłacik-Kramarczyk, A. Drabczyk, A. Kordyka, M. Godzierz, P. S. Wróbel, A. Tomala, B. Tyliszczak, A. Sobczak-Kupiec, Evaluation of the impact of pH of the reaction mixture, type of the stirring, and the reagents' concentration in the wet precipitation method on physicochemical properties of hydroxyapatite so as to enhance its biomedical application potential, J. Biomed. Mater. Res. 110 (2022) 2649–2666, https://doi.org/10.1002/jbm.b.35118.

[54] A. Hammouda, A. Canizarès, P. Simon, A. Boughalout, M. Kechouane, Improving the sensitivity of Raman signal of ZnO thin films deposited on silicon substrate, Vib. Spectrosc. 62 (2012) 217–221, https://doi.org/10.1016/j.vibspec.2012.07.004.

[55] A.M. Ali, A.A. Ismail, R. Najmy, A. Al-Hajry, Preparation and characterization of ZnO–SiO_2 thin films as highly efficient photocatalyst, J. Photochem. Photobiol. A Chem. 275 (2014) 37–46, https://doi.org/10.1016/j.jphotochem.2013.11.002.

[56] I. Martina, R. Wiesinger, D. Jembrih-Simbürger, M. Schreiner, Micro-raman characterisation of silver corrosion products: instrumental set up and reference database, E-Preservation Sci. 9 (2012) 1–8.

[57] Y. Zhao, Y. Xie, Y.Y. Hui, L. Tang, W. Jie, Y. Jiang, L. Xu, S.P. Lau, Y. Chai, Highly impermeable and transparent graphene as an ultra-thin protection barrier for Ag thin films, J. Mater. Chem. C 1 (2013) 4956, https://doi.org/10.1039/c3tc30743c.

[58] M. Fernández-Lizárraga, J. García-López, S.E. Rodil, R.M. Ribas-Aparicio, P. Silva-Bermudez, Evaluation of the biocompatibility and osteogenic properties of metal oxide coatings applied by magnetron sputtering as potential biofunctional surface modifications for orthopedic implants, Materials 15 (2022) 5240, https://doi.org/10.3390/ma15155240.

[59] G.-J. Chen, S.-R. Jian, J.-Y. Juang, Surface analysis and optical properties of Cu-Doped ZnO thin films deposited by radio frequency magnetron sputtering, Coatings 8 (2018) 266, https://doi.org/10.3390/coatings8080266.

[60] R. Bayati, R. Molaei, A. Richmond, S. Nori, F. Wu, D. Kumar, J. Narayan, J. G. Reynolds, C.L. Reynolds, Modification of properties of yttria stabilized zirconia epitaxial thin films by excimer laser annealing, ACS Appl. Mater. Interf. 6 (2014) 22316–22325, https://doi.org/10.1021/am506298y.

[61] V. Dave, H.O. Gupta, R. Chandra, Nanostructured hydrophobic DC sputtered inorganic oxide coating for outdoor glass insulators, Appl. Surf. Sci. 295 (2014) 231–239, https://doi.org/10.1016/j.apsusc.2013.12.153.

[62] E.P. Ivanova, V.K. Truong, J.Y. Wang, C.C. Berndt, R.T. Jones, I.I. Yusuf, I. Peake, H.W. Schmidt, C. Fluke, D. Barnes, R.J. Crawford, Impact of nanoscale roughness of titanium thin film surfaces on bacterial retention, Langmuir 26 (2010) 1973–1982, https://doi.org/10.1021/la902623c.

[63] Y.N. Slavin, J. Asnis, U.O. Häfeli, H. Bach, Metal nanoparticles: understanding the mechanisms behind antibacterial activity, J. Nanobiotechnol. 15 (2017) 65, https://doi.org/10.1186/s12951-017-0308-z.

[64] I. Matai, A. Sachdev, P. Dubey, S. Uday Kumar, B. Bhushan, P. Gopinath, Antibacterial activity and mechanism of Ag–ZnO nanocomposite on S. aureus and GFP-expressing antibiotic resistant E. coli, Colloids Surf. B: Biointerf. 115 (2014) 359–367, https://doi.org/10.1016/j.colsurfb.2013.12.005.

[65] C. Uruén, G. Chopo-Escuin, J. Tommassen, R.C. Mainar-Jaime, J. Arenas, Biofilms as promoters of bacterial antibiotic resistance and tolerance, Antibiotics 10 (2020) 3, https://doi.org/10.3390/antibiotics10010003.

[66] W. Zimmerli, P. Sendi, Orthopaedic biofilm infections, APMIS 125 (2017) 353–364, https://doi.org/10.1111/apm.12687.

[67] E.C. Rodríguez-Merchán, D.J. Davidson, A.D. Liddle, Recent strategies to combat infections from biofilm-forming bacteria on orthopaedic implants, Int. J. Mol. Sci. 22 (2021) 10243, https://doi.org/10.3390/ijms221910243.

[68] I.A. Hassan, I.P. Parkin, S.P. Nair, C.J. Carmalt, Antimicrobial activity of copper and copper(i) oxide thin films deposited via aerosol-assisted CVD, J. Mater. Chem. B 2 (2014) 2855–2860, https://doi.org/10.1039/C4TB00196F.

[69] K.-T. Chuang, H. Abdullah, S.-J. Leu, K.-B. Cheng, D.-H. Kuo, H.-C. Chen, J.-H. Chien, W.-T. Hu, Metal oxide composite thin films made by magnetron sputtering for bactericidal application, J. Photochem. Photobiol. A Chem. 337 (2017) 151–164, https://doi.org/10.1016/j.jphotochem.2017.01.012.

[70] S.R. Geetha, P. Dhivya, P.D. Raj, M. Sridharan, S.A. Princy, Studies on magnetron sputtered ZnO–Ag films: adhesion activity of *S. aureus*, Int. J. Nanosci. 16 (2017) 1650026, https://doi.org/10.1142/S0219581X16500265.

[71] V. Vibornijs, M. Zubkins, E. Strods, Z. Rudevica, K. Korotkaja, A. Ogurcovs, K. Kundzins, J. Purans, A. Zajakina, Analysis of antibacterial and antiviral properties of ZnO and Cu coatings deposited by magnetron sputtering: evaluation of cell viability and ROS production, Coatings 14 (2023) 14, https://doi.org/10.3390/coatings14010014.

[72] T.J. Brunner, P. Wick, P. Manser, P. Spohn, R.N. Grass, L.K. Limbach, A. Bruinink, W.J. Stark, In vitro cytotoxicity of oxide nanoparticles: comparison to asbestos, silica, and the effect of particle solubility, Environ. Sci. Technol. 40 (2006) 4374–4381, https://doi.org/10.1021/es052069i.

[73] S. Majeed, N.F.B. Bakhtiar, M. Danish, M.N. Mohamad Ibrahim, R. Hashim, Green approach for the biosynthesis of silver nanoparticles and its antibacterial and antitumor effect against osteoblast MG-63 and breast MCF-7 cancer cell lines, Sustain. Chem. Pharm. 12 (2019) 100138, https://doi.org/10.1016/j.scp.2019.100138.

[74] N.J. Hallab, C. Vermes, C. Messina, K.A. Roebuck, T.T. Glant, J.J. Jacobs, Concentration- and composition-dependent effects of metal ions on human MG-63 osteoblasts, J. Biomed. Mater. Res. 60 (2002) 420–433, https://doi.org/10.1002/jbm.10106.

[75] B. Li, X. Liu, F. Meng, J. Chang, C. Ding, Preparation and antibacterial properties of plasma sprayed nano-titania/silver coatings, Mater. Chem. Phys. 118 (2009) 99–104, https://doi.org/10.1016/j.matchemphys.2009.07.011.

[76] H.-L. Huang, M.-T. Tsai, Y.-Y. Chang, Y.-J. Lin, J.-T. Hsu, Fabrication of a Novel Ta(Zn)O thin film on titanium by magnetron sputtering and plasma electrolytic oxidation for cell biocompatibilities and antibacterial applications, Metals 10 (2020) 649, https://doi.org/10.3390/met10050649.

[77] D. Wojcieszak, M. Osekowska, D. Kaczmarek, B. Szponar, M. Mazur, P. Mazur, A. Obstarczyk, Influence of material composition on structure, surface properties and biological activity of nanocrystalline coatings based on Cu and Ti, Coatings 10 (2020) 343, https://doi.org/10.3390/coatings10040343.